



# Solving three-dimensional interface problems with immersed finite elements: A-priori error analysis

Ruchi Guo<sup>a</sup>, Xu Zhang<sup>b,\*</sup>

<sup>a</sup> Department of Mathematics, University of California at Irvine, Irvine, CA 92697, United States of America

<sup>b</sup> Department of Mathematics, Oklahoma State University, Stillwater, OK 74078, United States of America



## ARTICLE INFO

### Article history:

Available online 21 May 2021

### Keywords:

Three-dimensional interface problem

Unfitted mesh method

Immersed finite element

Optimal error estimation

## ABSTRACT

Immersed finite element methods are designed to solve interface problems on interface-unfitted meshes. However, most of the study, especially analysis, is mainly limited to the two-dimension case. In this paper, we provide an a priori analysis for the trilinear immersed finite element method to solve three-dimensional elliptic interface problems on Cartesian grids consisting of cuboids. We establish the trace and inverse inequalities for trilinear IFE functions for interface elements with arbitrary interface-cutting configuration. Optimal a priori error estimates are rigorously proved in both energy and  $L^2$  norms, with the constant in the error bound independent of the interface location and its dependence on coefficient contrast explicitly specified. Numerical examples are provided not only to verify our theoretical results but also to demonstrate the applicability of this IFE method in tackling some real-world 3D interface models.

© 2021 Elsevier Inc. All rights reserved.

## 1. Introduction

Interface problems are ubiquitous. Many real-world applications in fracture mechanics, fluid mechanics, and material science involve multiple mediums and can be considered as three-dimensional (3D) interface problems. For mathematicians and computational scientists, partial differential equations (PDEs) are often used to model these problems. Usually, these governing equations have discontinuous coefficients that represent the different material properties.

To solve interface problems, in general, there are two classes of numerical methods. The first class of methods uses interface-fitted meshes, i.e., the mesh must be tailored to fit the interface. Methods of this type include classical finite element method (FEM) [11], discontinuous Galerkin method [4], and virtual element method [10], to name only a few. The second class of numerical methods uses interface-unfitted meshes that are independent of the interface. Structured meshes such as the Cartesian mesh are often used in these methods. An immediate benefit of these unfitted-mesh methods is the avoidance of re-mesh when solving a dynamic problem with evolving interfaces. For example, this feature can be particularly advantageous in simulating multi-phase fluid flow [32], crystal growth [7], solving geometric inverse problems [21] and so on. We refer readers to [38] for various applications. Moreover, the mesh generation can be especially challenging in the 3D case since the geometry and topology can be rather complicated such as those in biomedical image [3] and geophysical image [13].

In the past few decades, there are many numerical methods introduced for solving interface problems based on unfitted meshes. In the finite difference framework, there are Peskin's immersed boundary method [45], immersed interface method

\* Corresponding author.

E-mail addresses: [ruchig@uci.edu](mailto:ruchig@uci.edu) (R. Guo), [xzhang@okstate.edu](mailto:xzhang@okstate.edu) (X. Zhang).

[36], matched interface and boundary method [52], to name only a few. In the framework of finite element methods (FEMs), there are general FEM [6], Cut-FEM [8], multi-scale FEMs [12,33], extended FEM [14], partition of unity method [43], and immersed FEM [37], etc.

The immersed FEM was first developed in [37] for solving one-dimensional (1D) elliptic interface problem, in which the lowest order IFE function was developed and analyzed. The fundamental idea is to construct some special shape functions capturing the jump behavior of the exact solution. Since then, IFE methods have been extended to higher-order approximation [2,9] in 1D, and two-dimensional (2D) interface problems [18,19,24,28,40,41], and 3D interface problems [35,48,26,20]. Besides the classical second-order elliptic equation, IFE methods have been applied in a wide variety of interface problems, such as the linear elasticity system [42,22], moving interface problems [17,30,39], interface inverse problems [21], and stochastic interface models [51].

So far, most of IFE methods in literature deal with 2D interface problems. Very few tackles the real 3D interface problems. In [35], a linear IFE method was introduced on unfitted tetrahedral meshes, and was then used in [26] for simulating plasma–lunar surface interactions. In [48], a trilinear element was introduced on cuboidal mesh for solving the electroencephalography forward problem. However, there are no theoretical results for either of these methods. Recently, in [20], the authors reconstructed trilinear IFE functions on cuboidal meshes based on the actual interface surface. The unisolvency of the trilinear IFE functions was shown using the invertibility of a Sherman–Morrison matrix. A maximum angle condition was employed in the construction procedure to guarantee the optimal approximation capabilities of the trilinear IFE spaces, and rigorous proof was also given through detailed geometrical analysis. However, the error analysis of the IFE solution is still open in the 3D case.

As most of the IFE spaces in the literature, the global IFE functions in [20] are discontinuous across interface faces, which can cause certain nonconformity and loss of convergence order if the standard Galerkin scheme is used. We shall demonstrate by numerical results that the standard Galerkin scheme used in the literature aforementioned for 3D IFE cannot achieve optimal accuracy in general due to the discontinuity on interface faces. The partially penalized IFE (PPIFE) scheme has been widely used to address this issue [40,22] in 2D situation, and the basic idea is to use interior penalties to handle discontinuities only on interface edges/faces. The PPIFE method was first introduced in [40] for the 2D elliptic interface problem in which the analysis relies on piecewise  $H^3$  regularity of the solution. Recently, through interpolation error analysis on patches of interface elements, it was proved in [23] that the errors decay optimally in both energy norm and  $L^2$  norm requiring only the piecewise  $H^2$  regularity of the solution.

This paper has two major contributions. The first one is to conduct a rigorous error analysis for the PPIFE method for 3D interface problems. The global degrees of freedom for the proposed IFE method are isomorphic to the standard continuous piecewise trilinear finite element space defined on the same mesh which is independent of the interface location and advantageous for moving interface problems. But due to the complexity of the geometrical configurations of interface elements and the corresponding IFE functions, the analysis can be very challenging. For example, fundamental inequalities such as trace inequality and inverse inequality must be re-established for three-dimensional IFE functions. Nevertheless, the standard theoretical tools can barely be used due to the low regularity of the solution. In our analysis, we show the discrete extension operator used to construct IFE functions is stable regardless of interface location, and this stability serves as the foundation of the trace and inverse inequalities, which is also the key for the proposed PPIFE method to be stable for an arbitrary interface. Another challenge is the inconsistency of the numerical scheme due to the discontinuity of the trilinear IFE function across the interface surface. Thanks to the optimal error bound of the interpolation operator [20], we are able to show that the inconsistency term will not affect the overall accuracy, namely, there is no need to add penalties on the interface surface. The second contribution is the extensive investigation of the applicability of the proposed IFE method. In particular, we demonstrate that it can be used to solve problems with various interface shapes and topologies. Moreover, we also investigate the implementation of the method for some real-world interface models where only the original cloud-point geometric data on the interface are available. In a realistic simulation, these raw data need to be used to generate a computational interface surface which can be further utilized by the proposed IFE method.

The rest of the paper is organized as follows. In Section 2, we present the three-dimensional interface problem and recall some geometrical properties of the 3D cuboidal meshes with interface surfaces. In Section 3, we present the trilinear IFE spaces and the PPIFE method for solving 3D interface problems. In Section 4, we prove fundamental inequalities including the trace and inverse inequalities of the trilinear IFE functions. In Section 5, we derive the *a priori* error estimates of PPIFE solutions in both energy norm and  $L^2$  norm. In Section 6, we present extensive numerical experiments not only to verify our theoretical results but also to demonstrate how this IFE method can be applied to tackle real-world 3D interface problems. A brief conclusion will be drawn in Section 7.

## 2. Interface models and preliminary results

Let  $\Omega \subseteq \mathbb{R}^3$  be an open bounded domain. Without loss of generality, we assume that  $\Omega$  is separated into two subdomains  $\Omega^-$  and  $\Omega^+$  by a closed  $C^2$  manifold  $\Gamma \subseteq \Omega$  known as the interface. These subdomains contain different materials identified by a piecewise constant function  $\beta(\mathbf{x})$  which is discontinuous across the interface  $\Gamma$ , i.e.,

$$\beta(\mathbf{x}) = \begin{cases} \beta^- & \text{in } \Omega^-, \\ \beta^+ & \text{in } \Omega^+, \end{cases}$$

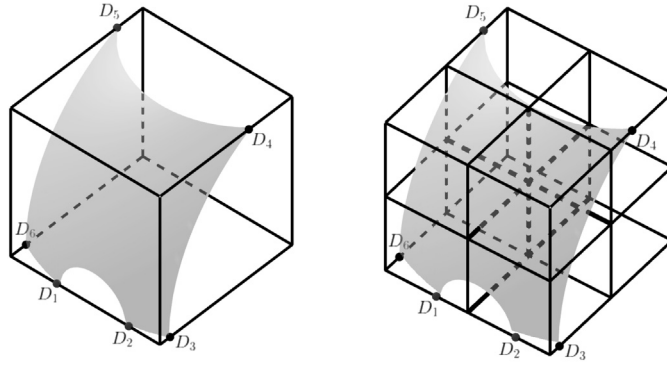


**Fig. 1.** Refine an interface element into eight congruent elements. Left: an interface element with an edge containing two intersection points (left). Right: a further partition such that this element satisfies the hypothesis **(H3)**.

where  $\beta^\pm > 0$  and  $\mathbf{x} = (x, y, z)$ . Throughout the analysis, we assume  $\beta^+ > \beta^-$ . We consider the following interface problem of the elliptic type on  $\Omega$ :

$$-\nabla \cdot (\beta \nabla u) = f, \quad \text{in } \Omega^- \cup \Omega^+, \tag{2.1a}$$

$$[[u]]_\Gamma = 0, \quad \text{on } \Gamma, \tag{2.1b}$$

$$[[\beta \nabla u \cdot \mathbf{n}]]_\Gamma = 0, \quad \text{on } \Gamma, \tag{2.1c}$$

$$u = g, \quad \text{on } \partial\Omega, \tag{2.1d}$$

where  $[[v]]_\Gamma := (v|_{\Omega^+})_\Gamma - (v|_{\Omega^-})_\Gamma$ , and  $\mathbf{n}$  is the unit normal vector of  $\Gamma$  from  $\Omega^+$  to  $\Omega^-$ . For simplicity, we denote  $u^s = u|_{\Omega^s}$ ,  $s = \pm$ , in the rest of this article. Here we only consider the homogeneous jump condition, and the nonhomogeneous case can be treated by some enriched functions through the framework recently developed by Babuška et al. in [1].

In this section, we first introduce some Sobolev spaces used throughout this article and recall some geometrical properties of the unfitted mesh for three-dimensional interface problems. Given an open subset  $\tilde{\Omega} \subseteq \Omega$ , let  $H^k(\tilde{\Omega})$  be the standard Hilbert spaces on  $\tilde{\Omega}$  with the norm  $\|\cdot\|_{k, \tilde{\Omega}}$  and the semi-norm  $|\cdot|_{k, \tilde{\Omega}}$ . In the case  $\tilde{\Omega}^s := \tilde{\Omega} \cap \Omega^s \neq \emptyset$ ,  $s = \pm$ , we define the splitting Hilbert spaces

$$PH^k(\tilde{\Omega}) = \{u \in H^k(\tilde{\Omega}^\pm) : [[u]]_{\Gamma \cap \tilde{\Omega}} = 0 \text{ and } [[\beta \nabla u \cdot \mathbf{n}]]_{\Gamma \cap \tilde{\Omega}} = 0\}, \tag{2.2}$$

where the definition implicitly implies the involved traces on  $\Gamma \cap \tilde{\Omega}$  are well defined, with the associated norms and semi-norms defined as follows

$$\|\cdot\|_{PH^k(\tilde{\Omega})}^2 := \|\cdot\|_{H^k(\tilde{\Omega}^+)}^2 + \|\cdot\|_{H^k(\tilde{\Omega}^-)}^2, \quad |\cdot|_{PH^k(\tilde{\Omega})}^2 := |\cdot|_{H^k(\tilde{\Omega}^+)}^2 + |\cdot|_{H^k(\tilde{\Omega}^-)}^2.$$

In the following, we assume that  $\Omega \subset \mathbb{R}^3$  is a cuboid domain, and  $\mathcal{T}_h$  is a Cartesian cuboidal mesh of  $\Omega$  where  $h$  denotes the maximum length of all the cuboids. Denote  $\mathcal{F}_h$ ,  $\mathcal{E}_h$  and  $\mathcal{N}_h$  as the collections of faces, edges, and nodes, respectively. We call an element  $T \in \mathcal{T}_h$  an interface element if not all of its vertices locate on the same side of the interface  $\Gamma$ ; otherwise, we treat it as a non-interface element. Similarly, we can define the interface faces and interface edges by the relative location of its vertices with the interface. Note that non-interface elements/faces/edges may still intersect with the interface due to large curvature of the segment of the interface, see the illustration in Fig. 1. However, this issue can always be resolved by refining the mesh. Let  $\mathcal{T}_h^i/\mathcal{F}_h^i/\mathcal{E}_h^i$  and  $\mathcal{T}_h^n/\mathcal{F}_h^n/\mathcal{E}_h^n$  be the collections of interface and non-interface elements/faces/edges, respectively. Let  $\kappa$  be the maximal curvature (principle curvature) of the interface surface  $\Gamma$ . Moreover, for each interface element  $T \in \mathcal{T}_h^i$ , we define its patch  $\omega_T$  as

$$\omega_T = \{T' \in \mathcal{T}_h : \overline{T'} \cap \overline{T} \neq \emptyset\}. \tag{2.3}$$

Many unfitted-mesh methods rely on the assumption that the mesh size is sufficiently small such that the interface curve/surface is resolved enough [18,27]. In this section, we provide a delicate approach to quantify how well the interface is resolved by a fixed mesh. In particular, our approach is to measure the flatness of the interface within each interface element in terms of the maximal angle between the normal vectors of the interface surface and its planar approximation. These fundamental geometric results will be used throughout this paper. First of all, we recall the so-called  $r$ -tubular neighborhood of a smooth manifold from [15] which is a very useful concept in computational geometry [44].

**Lemma 2.1** (*r-tubular neighborhood*). *Given a smooth compact surface  $\Gamma$  in  $\mathbb{R}^3$ , for each point  $X \in \Gamma$ , let  $N_X(r)$  be a segment with the length  $2r$  centered at  $X$  and perpendicular to  $\Gamma$ . Then, there exists a positive  $r > 0$  such that  $N_X(r) \cap N_Y(r) = \emptyset$  for any  $X, Y \in \Gamma$ ,  $X \neq Y$ . Then the  $r$ -tubular neighborhood of  $\Gamma$  is defined as the set  $U_\Gamma(r) = \cup_{X \in \Gamma} N_X(r)$ .*

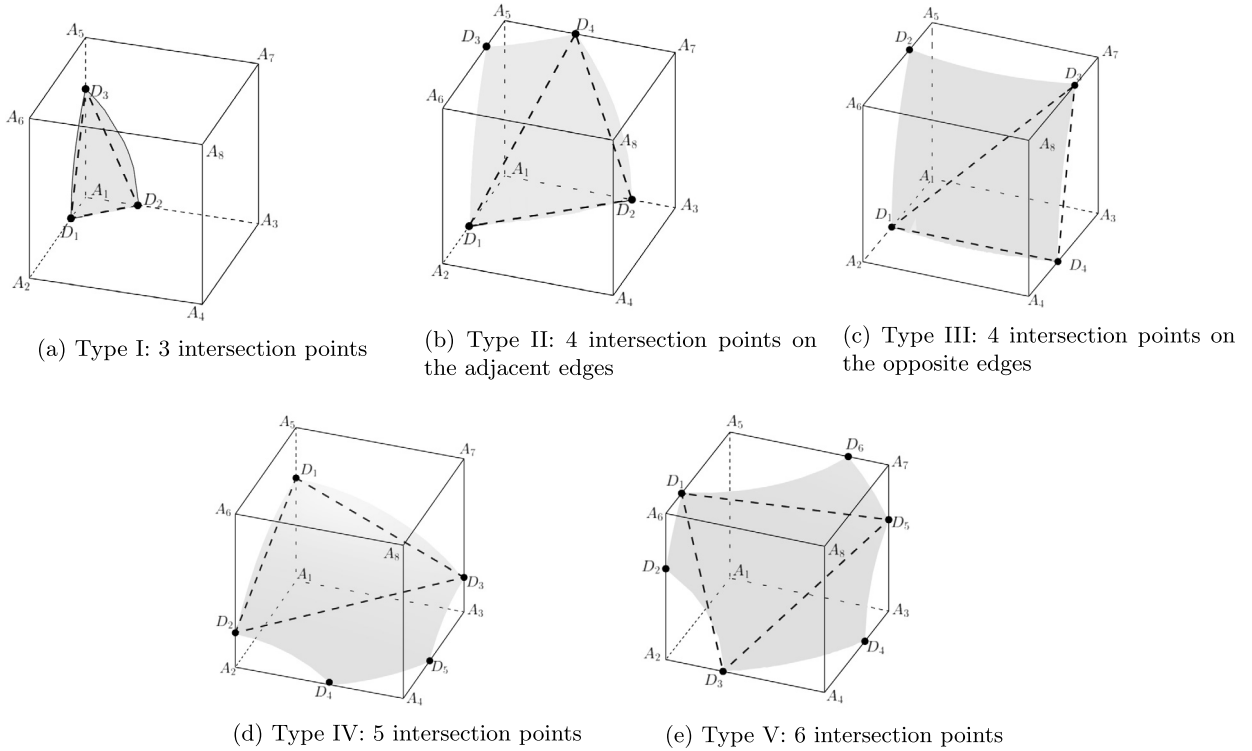


Fig. 2. Possible Interface Element Configuration.

Define  $r_\Gamma$  to be the largest  $r$  such that Lemma 2.1 holds, namely it corresponds to the largest  $r$ -tabular neighborhood, and this positive number  $r_\Gamma$  is referred as the reach of the surface  $\Gamma$  [44]. We further note that the reach  $r_\Gamma$  is only determined by the surface itself. Throughout this paper, we assume that the mesh size  $h$  is sufficiently small such that the following hypotheses hold [20]:

- (H1)  $h < r_\Gamma / (3\sqrt{3})$ .
- (H2)  $h\kappa \leq 0.0288$ .
- (H3) The interface  $\Gamma$  cannot intersect an edge  $e \in \mathcal{E}_h$  at more than one point.
- (H4) The interface  $\Gamma$  cannot intersect a face  $f \in \mathcal{F}_h$  at more than two edges.

These hypotheses basically ensure that the interface surface is sufficiently resolved by the unfitted mesh such that it is flat enough inside each interface element. Similar assumptions have been used in many unfitted-mesh methods such as [8,25,18,27,35]. In this work we make the bounds in (H1) and (H2) explicit and computable which can guide the mesh generation in real computation. We refer readers to [20] for more details of calculation of those bounds.

Now we are ready to describe the classification of the interface elements. Based on hypotheses (H3) and (H4), we claim that the interface surface can only intersect an element at six points at the most. In fact, suppose that an element has seven intersection points. According to (H3), these seven points must be on seven different edges. Since every edge is shared by two adjacent faces in the element, there is a total of fourteen interface edges, counting each edge twice from its sharing faces. A cuboid has six faces in total, which means there is at least one face containing at least three interface edges. This is contradicted to (H4).

According to [20], when the interface is resolved sufficiently by an unfitted mesh, there are only five possible interface element configurations as shown in Fig. 2. Taking into account the rotation, the five types of interface cuboids have the following representatives:

- Type I interface element:** three intersection points on three edges
- Type II interface element:** four intersection points on four parallel edges
- Type III interface element:** four intersection points on two pairs of adjacent edges
- Type IV interface element:** five intersection points on five edges
- Type V interface element:** six intersection points on six edges

See Fig. 2 (a-e) for illustrations of all types of interface elements. This classification strategy can also be used in computation to efficiently determine the geometry configuration of each interface element by counting the number of interface points and the number of vertices on each side. The classification of interface elements is important in constructing IFE functions and numerical quadrature which we shall discuss later on.

Now we describe how to construct an approximate plane, denoted by  $\tau_T$ , for each interface element  $T \in \mathcal{T}_h^i$  with sufficient geometric representation for the interface. This is done by constructing a triangle formed by three suitable intersection points such that its maximal angle is always bounded by  $135^\circ$  regardless of the interface location [20]. As shown by Fig. 2, we follow the choice in [20] to make this plane  $\tau_T$  contain the following triangles:  $\Delta D_1 D_2 D_3$  for Type I,  $\Delta D_1 D_2 D_4$  for Type II,  $\Delta D_1 D_4 D_3$  for Type III,  $\Delta D_1 D_2 D_3$  for Type IV and  $\Delta D_1 D_3 D_5$  for Type V. We emphasize that the choice may not be unique, and any triangle is acceptable as long as the maximal angle condition is satisfied. We refer readers to [10,20] for more details on the calculation of the maximal angles of these triangles. Note that the maximal angle condition is also widely used in standard finite element analysis, which can be traced back to the early works of Babuška [5]. Under this choice of the plane  $\tau_T$ , we recall from [20] the following optimal geometric error estimate.

**Theorem 2.2.** *Let  $\mathcal{T}_h$  be a Cartesian mesh whose mesh size is small enough such that (H1)-(H4) hold, then the following estimates hold for every point  $X \in \Gamma \cap T$  (or every point  $X \in \Gamma \cap \omega_T$ ):*

$$\|X - X_\perp\| \leq 12.0927\kappa h^2, \tag{2.4a}$$

$$\mathbf{n}(X) \cdot \bar{\mathbf{n}} \geq 1 - 26.6121\kappa^2 h^2, \tag{2.4b}$$

where  $X_\perp$  is the projection of  $X$  onto  $\tau_T$ ,  $\mathbf{n}(X)$  is the unit normal vector to  $\Gamma$  at  $X$ , and  $\bar{\mathbf{n}}$  is the normal vector to  $\tau_T$ .

**Proof.** See the proof of Theorem 2.2 of [20].  $\square$

A direct consequence of Theorem 2.2 is the following lemma.

**Lemma 2.3.** *Under the conditions of Theorem 2.2, there exists a constant  $C$  independent of interface location and mesh size  $h$  such that  $meas(\Gamma \cap T) \leq Ch^2$ .*

**Proof.** Clearly, we have  $meas(\tau_T) \leq Ch^2$ . Then using (2.4b) we have

$$meas(\Gamma \cap T) = \left| \int_{\Gamma \cap T} dS \right| = \left| \int_{\tau_T} \frac{1}{\mathbf{n}(X) \cdot \bar{\mathbf{n}}} dS \right| \leq Ch^2.$$

Finally, for simplicity's sake, we shall employ a generic constant  $C$  in the rest of this article which is independent of interface location, mesh size, and discontinuous coefficients  $\beta^\pm$  without explicitly mentioning in the presentation. In addition, the notation  $\simeq$  denotes equivalence where the hidden constant  $C$  has the same property.  $\square$

### 3. Trilinear IFE spaces and the IFE method

In this section, we describe the trilinear IFE functions and the PPIFE method. In general, IFE functions constructed by piecewise polynomials cannot satisfy the jump conditions exactly for an arbitrary interface surface. Different approximations of jump conditions have been proposed in the 2D case, see [18,19,29]. Most of the methods rely on the linear approximation of the interface curve constructed by simply connecting the intersection points, and then the approximate jump conditions are posed on this line. However, this approach becomes obscure in the 3D case since the intersection points, the number varying from three to six, may not be coplanar. Some early works of IFE functions use the approximation plane passing through the three points which have the shortest distance to the others for which we refer readers to [26,35] for details. Besides, a level-set approximate approach was used in [48]. But to our best knowledge, these works on 3D IFE functions are in lack of theoretical foundation. Recently, the authors in [20] proposed a new and provable construction approach by using a special approximate plane satisfying the maximal angle condition described above.

Let  $\mathbb{Q}_1 = \text{Span}\{1, x, y, z, xy, xz, yz, xyz\}$  be the trilinear polynomial space and let  $F$  be the centroid of the triangle described above and shown in Fig. 2. According to [20], the local trilinear IFE space  $S_h(T)$  is formed by piecewise polynomials  $\phi_T$  with  $\phi_T^\pm = \phi_T|_{T^\pm} \in \mathbb{Q}_1$  which satisfy the approximate jump conditions to (2.1b) and (2.1c):

$$\phi_T^-|_{\tau_T} = \phi_T^+|_{\tau_T}, \quad \mathbf{d}(\phi_T^-) = \mathbf{d}(\phi_T^+), \tag{3.1a}$$

$$\beta^- \nabla \phi_T^-(F) \cdot \bar{\mathbf{n}} = \beta^+ \nabla \phi_T^+(F) \cdot \bar{\mathbf{n}}, \tag{3.1b}$$

where  $\mathbf{d}(p)$  is the vector of coefficients of terms  $xy, yz, xz$  and  $xyz$  in a polynomial  $p \in \mathbb{Q}_1$ . Then, on each interface element, we recall the extension operator  $\mathcal{C}_T$  from (3.4) in [20]:

$$C_T : \mathbb{Q}_1 \rightarrow \mathbb{Q}_1, \text{ such that } \phi_T^- = p \in \mathbb{Q}_1 \text{ and } \phi_T^+ = C_T(p) \in \mathbb{Q}_1 \tag{3.2}$$

together satisfy the approximate jump conditions (3.1).

Let  $L(X) = (X - F) \cdot \bar{\mathbf{n}}$  be the level-set function of the plane  $\tau_T$ . In particular, we have the following explicit expression for the operator:

$$C_T(p) = p + \left( \frac{\beta^-}{\beta^+} - 1 \right) (\nabla p(F) \cdot \bar{\mathbf{n}}) L, \tag{3.3a}$$

$$C_T^{-1}(p) = p + \left( \frac{\beta^+}{\beta^-} - 1 \right) (\nabla p(F) \cdot \bar{\mathbf{n}}) L. \tag{3.3b}$$

Then the proposed IFE space  $S_h(T)$  can be written as

$$S_h(T) = \{\phi_T|_{T^\pm} \in \mathbb{Q}_1 : \phi_T|_{T^-} = p \in \mathbb{Q}_1 \text{ and } \phi_T|_{T^+} = C_T(p)\}, \quad \forall T \in \mathcal{T}_h^i. \tag{3.4}$$

It is crucial in both analysis and computation which shape functions are used, namely which degrees of freedom are chosen. Different shape functions may have different features in computation. In this article, we consider the Lagrange IFE shape function  $\phi_{i,T}$  such that

$$\phi_{i,T}(A_j) = \delta_{i,j}, \quad i, j = 1, \dots, 8, \tag{3.5}$$

where  $A_j$  are the vertices of the interface element  $T$  as shown in Fig. 2. Then the IFE space can be rewritten as

$$S_h(T) = \text{Span}\{\phi_{i,T} : i = 1, \dots, 8\}. \tag{3.6}$$

The global IFE space is defined as

$$S_h(\Omega) = \{v \in L^2(\Omega) : v|_T \in S_h(T) \forall T \in \mathcal{T}_h, \text{ and } v \text{ is continuous at } X \in \mathcal{N}_h\}. \tag{3.7}$$

It has been shown in [20] that these IFE spaces have optimal approximation capabilities to the functions satisfying the jump conditions in the  $L^2$  and  $H^1$  norms. We shall discuss some new approximation capabilities in Section 5. Let  $S_h^0(\Omega)$  be the subspace of  $S_h(\Omega)$  with zero trace on  $\partial\Omega$ . Clearly,  $S_h^0(\Omega)$  is a subspace of the underlying space

$$V_h(\Omega) = \{v \in L^2(\Omega) : v|_T \in H^1(T) \forall T \in \mathcal{T}_h^n, \text{ and } v|_{T^\pm} \in H^1(T^\pm) \forall T \in \mathcal{T}_h^i, \\ v \text{ is continuous at each } X \in \mathcal{N}_h \text{ and } e \in \mathcal{E}_h^n, v|_{\partial\Omega} = 0\}. \tag{3.8}$$

Now the proposed PPIFE method is: find  $u_h \in S_h(\Omega)$  such that  $u_h(X) = g(X) \forall X \in \mathcal{N}_h \cap \partial\Omega$  and

$$a_h(u_h, v_h) = L(v_h), \quad \forall v_h \in S_h^0(\Omega), \tag{3.9}$$

where the bilinear form  $a_h(\cdot, \cdot)$  is given by

$$a_h(u, v) = \sum_{T \in \mathcal{T}_h} \int_T \beta \nabla u \cdot \nabla v dX - \sum_{F \in \mathcal{F}_h^i} \int_F \{\beta \nabla u \cdot \mathbf{n}\} \llbracket v \rrbracket dS \\ + \epsilon \sum_{F \in \mathcal{F}_h^i} \int_F \{\beta \nabla v \cdot \mathbf{n}\} \llbracket u \rrbracket dS + \sum_{F \in \mathcal{F}_h^i} \frac{\sigma}{h} \int_F \llbracket u \rrbracket \llbracket v \rrbracket dS, \tag{3.10}$$

with  $\sigma = \bar{\sigma}^0 (\beta^+)^2 / \beta^-$  with  $\bar{\sigma}^0$  large enough but independent of  $h$  and  $\beta^\pm$ , and the linear form  $L : S_h(\Omega) \rightarrow \mathbb{R}$  is

$$L(v) = \int_\Omega f v dX. \tag{3.11}$$

Here,  $\llbracket \cdot \rrbracket_F$  and  $\{\cdot\}_F$  denote the jump and the average, respectively, of a function on a face  $F$  from two neighboring elements  $T_F^1$  and  $T_F^2$  sharing the face  $F$ , i.e.,

$$\llbracket w \rrbracket_F = (w|_{T_F^1})|_F - (w|_{T_F^2})|_F, \quad \{w\}_F = \frac{1}{2} \left( (w|_{T_F^1})|_F + (w|_{T_F^2})|_F \right).$$

For simplicity, we omit the subscript  $F$ , if there is no confusion on where the jump or average is defined.

To show how the exact solution is related to this scheme, we prove the following identity.

**Lemma 3.1.** Let  $u$  be the solution to (2.1). Then the following error equation holds

$$a_h(u, v_h) - b_h(u, v_h) = \int_{\Omega} f v_h dX, \quad \forall v_h \in S_h(\Omega), \tag{3.12}$$

where

$$b_h(u, v_h) = \sum_{T \in \mathcal{T}_h^i} \int_{T \cap \Gamma} \beta \nabla u \cdot \mathbf{n} \llbracket v_h \rrbracket dS. \tag{3.13}$$

**Proof.** We multiply (2.1a) by  $v_h \in S_h(\Omega)$  and integrate over an interface element  $T$ . Apply the Green’s formula, then we obtain

$$\begin{aligned} \int_T -\nabla \cdot (\beta \nabla u) v_h dX &= \int_T \beta \nabla u \cdot \nabla v_h dX - \int_{\partial T^-} (\beta \nabla u \cdot \mathbf{n}_{T^-}) v_h dS - \int_{\partial T^+} (\beta \nabla u \cdot \mathbf{n}_{T^+}) v_h dS \\ &= \int_T \beta \nabla u \cdot \nabla v_h dX - \int_{\partial T} (\beta \nabla u \cdot \mathbf{n}_T) v_h dS - \int_{T \cap \Gamma} (\beta \nabla u \cdot \mathbf{n}) \llbracket v_h \rrbracket dS \end{aligned} \tag{3.14}$$

where  $\mathbf{n}_{T^+}$ ,  $\mathbf{n}_{T^-}$ , and  $\mathbf{n}_T$  are the outward normal to  $T^+$ ,  $T^-$ , and  $T$ , respectively. Note that the normal vector of interface  $\mathbf{n} = \mathbf{n}_{T^+} = -\mathbf{n}_{T^-}$ . The last equality is due to the homogeneous flux jump condition (2.1c). The identities on non-interface elements are trivial as there is no interface. Now, adding these identities for all elements and noticing that IFE functions are continuous across all the non-interface faces and discontinuous across interface faces, we obtain

$$\sum_{T \in \mathcal{T}_h^i} \int_T \beta \nabla u \cdot \nabla v_h dX - \sum_{F \in \mathcal{F}_h^i} \int_F \{\beta \nabla u \cdot \mathbf{n}\} \llbracket v_h \rrbracket dS - \sum_{T \in \mathcal{T}_h^i} \int_{T \cap \Gamma} \beta \nabla u \cdot \mathbf{n} \llbracket v_h \rrbracket dS = \int_{\Omega} f v_h dX. \tag{3.15}$$

Finally, we note that  $\llbracket u \rrbracket = 0$  on each face  $F$  as  $u$  is the exact solution, which yields those two extra penalty terms involving  $\epsilon$  and  $\sigma$  in the bilinear form (3.10), and thus (3.12) is obtained.  $\square$

**Remark 3.2.** The inconsistency term  $b_h(u, v_h)$  in (3.13) is solely due to the planar geometrical approximation  $L$  of  $T \cap \Gamma$ . Consequently, if the interface surface  $T \cap \Gamma$  is a plane, there is no inconsistency error, i.e.,  $b_h(u, v_h) = 0$ .

**Remark 3.3.** We emphasize that (3.9) is not a discontinuous Galerkin (DG) scheme since the global IFE functions in (3.7) are all continuous at the mesh nodes such that the global degrees of freedom are isomorphic to the standard continuous piecewise trilinear finite element space. The penalties in (3.10) are only added on the interface faces to handle the discontinuities of IFE functions across the element boundaries. This isomorphism makes the IFE method advantageous when solving moving interface problems [39]. Meanwhile, the proposed scheme (3.9), as well as its derivation, is close to the interior penalty DG scheme [46]. The  $\epsilon$  term in (3.10) is to enforce certain desirable structure for the scheme [46].  $\epsilon = -1, 0, 1$  corresponds to the symmetric PPIFE (SPPIFE), the incomplete PPIFE (IPPIFE), and the non-symmetric PPIFE (NPPIFE) method, respectively. The  $\sigma$  term in (3.10) is to enforce the coercivity. Note that these two terms vanish when  $u$  is the exact solution.

#### 4. Trace and inverse inequalities

In this section, we proceed to establish the trace and inverse inequalities of the trilinear IFE functions. We note that these inequalities are non-trivial since IFE functions as piecewise polynomials do not have sufficient regularity for classical results to be applied. We need to consider all interface element configurations in Fig. 2 separately. However, we note that their analysis is mathematically similar to each other; thus, without loss of generality, we only consider the Type III interface element as shown in Fig. 2(c) since it is a good representative of our arguments.

We begin with a norm equivalence for polynomials on interface elements. For each interface element  $T$ , we denote the subelements cut by the interface  $\Gamma$  by  $T_1$  and  $T_2$  where  $T_1$  contains the vertex  $A_1$  and  $T_2$  contains the vertex  $A_8$ . Similarly, we have the subelements  $\tilde{T}_1$  and  $\tilde{T}_2$  cut by the approximating plane  $\tau_T$ . Then we have the following results.

**Lemma 4.1.** On an interface element  $T$ , the following norm equivalence holds

$$\| \cdot \|_{L^2(T_1)} \simeq \| \cdot \|_{L^2(\tilde{T}_1)} \simeq \| \cdot \|_{L^2(T)}, \quad \text{on } \mathbb{Q}_1, \tag{4.1}$$

for the interface element types:

- Type III in Fig. 2, if  $|A_4 D_4| \leq \frac{1}{2} |A_4 A_3|$  or  $|A_2 D_1| \leq \frac{1}{2} |A_2 A_1|$  or  $|A_6 D_2| \leq \frac{1}{2} |A_6 A_5|$  or  $|A_8 D_3| \leq \frac{1}{2} |A_8 A_7|$ ;

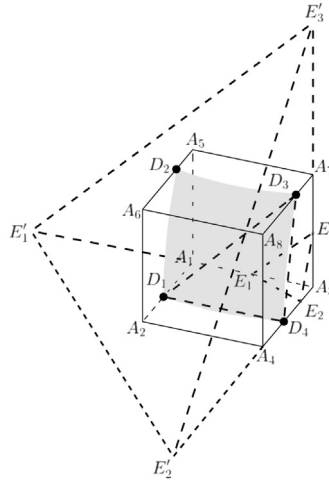


Fig. 3. Type III interface element inclusion.

- Type V in Fig. 2.

In addition, the following norm equivalence holds

$$\| \cdot \|_{L^2(T_2)} \simeq \| \cdot \|_{L^2(\tilde{T}_2)} \simeq \| \cdot \|_{L^2(T)}, \quad \text{on } \mathbb{Q}_1, \tag{4.2}$$

for the interface element types:

- Type I and Type II in Fig. 2;
- Type III in Fig. 2 if  $|A_4D_4| \geq \frac{1}{2}|A_4A_3|$  or  $|A_2D_1| \geq \frac{1}{2}|A_2A_1|$  or  $|A_6D_2| \geq \frac{1}{2}|A_6A_5|$  or  $|A_8D_3| \geq \frac{1}{2}|A_8A_7|$ ;
- Type IV and Type V in Fig. 2.

**Proof.** Without loss of generality, we consider the Type III interface element in Fig. 2(c), and only prove (4.1). In this case the approximate plane  $\tau_T$  passing through any three points of  $D_1, D_2, D_3$  and  $D_4$  has the geometric approximation given in Theorem 2.2; and thus by symmetricity, without loss of generality, we only need to consider the case  $|A_4D_4| \leq \frac{1}{2}|A_4A_3|$ . First of all, the hypothesis (H2) and (2.4a) indicate that

$$\text{dist}(\tau_T, \Gamma \cap T) \leq 12.0927(\kappa h)h \leq 0.3386h. \tag{4.3}$$

We then consider the pyramid  $A_3E_1E_2E_3$  denoted by  $P_1$  with  $E_1, E_2$  and  $E_3$  satisfying  $|A_3E_3|/|A_3A_7| = |A_3E_1|/|A_3A_1| = 1/10$  and  $|A_3E_2|/|A_3A_4| = 1/20$  as shown in Fig. 3. We can directly calculate that the shortest distance from  $E_1, E_2$  and  $E_3$  to the plane  $\tau_T$  is  $\sqrt{1/6} \cdot 0.9h = 0.3674h > 0.3386h$ . Hence, (4.3) shows that  $E_1, E_2$  and  $E_3$  are all in  $T_1$ , and thus the pyramid  $A_3E_1E_2E_3$  is always inside  $T_1$  regardless of the interface location. Therefore, we can construct a new pyramid  $A_3E'_1E'_2E'_3$  denoted by  $P'_1$  such that it is homothetic to  $P_1$  and always contains the cubic element  $T$ , as illustrated by Fig. 3. By Lemma 2.2 in [49], we have for any  $v \in \mathbb{Q}_1$ , there holds

$$\|v\|_{L^2(T)} \leq C\|v\|_{L^2(P'_1)} \leq C\|v\|_{L^2(P_1)} \leq C\|v\|_{L^2(T_1)}. \tag{4.4}$$

Clearly, the pyramid  $P_1$  must be always inside the subelement  $\tilde{T}_1$ , then by similar derivation to (4.4), we still have  $\|v\|_{L^2(T)} \leq C\|v\|_{L^2(\tilde{T}_1)}$ . Using the simple geometry, we immediately have

$$\|v\|_{L^2(T_1)} \leq C\|v\|_{L^2(T)}, \quad \text{and} \quad \|v\|_{L^2(\tilde{T}_1)} \leq C\|v\|_{L^2(T)}.$$

Combining these estimates, we arrive at (4.1).  $\square$

Next we prove the following kind of trace inequality on a pyramid.

**Lemma 4.2.** Given a pyramid  $K$  with a convex polygonal base  $B$ , suppose  $B$  has  $N_B$  edges, then

$$\|p(X_0)\| \leq CN_B^{1/2}|K|^{-1/2}\|p\|_{L^2(K)}, \quad \forall p \in \mathbb{Q}_1, \quad \forall X_0 \in B. \tag{4.5}$$

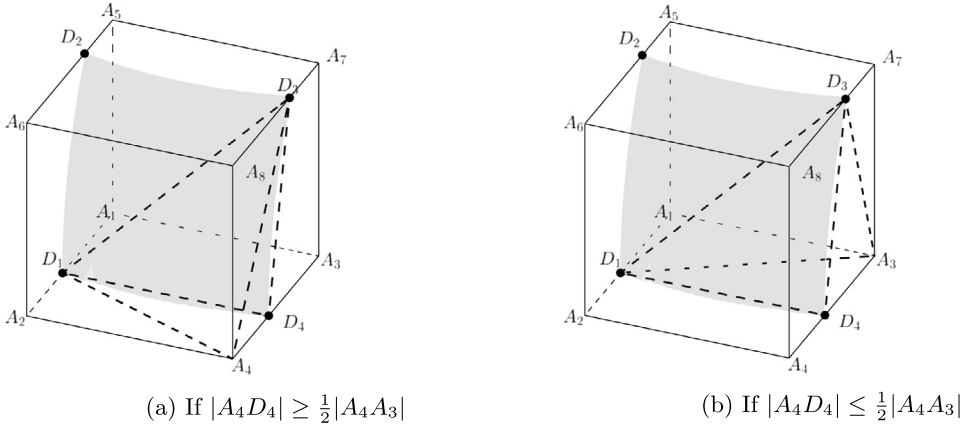


Fig. 4. Proof of Lemmas 4.3 and 4.4.

**Proof.** We connect  $X_0$  and the vertices of  $B$ , and thus obtain  $N_B$  triangles denoted by  $\Delta_i, i = 1, \dots, N_B$ . Then we connect  $X_0$  and the apex of the pyramid to obtain  $N_B$  sub-pyramids denoted by  $K_i, i = 1, \dots, N_B$ . Without loss of generality, we assume  $|K_1| \geq |K_2| \geq \dots \geq |K_{N_B}|$ . Then  $|K| = \sum_{i=1}^{N_B} |K_i| \leq N_B|K_1|$ . Thus, on  $K_1$ , the standard trace inequality for polynomials [50] yields

$$|p(X_0)| \leq C|\Delta_1|^{-1/2} \|p\|_{L^2(\Delta_1)} \leq C|\Delta_1|^{-1/2} \left(\frac{|\Delta_1|}{|K_1|}\right)^{1/2} \|p\|_{L^2(K_1)} \leq CN_B^{1/2} |K|^{-1/2} \|p\|_{L^2(K)}. \quad \square \quad (4.6)$$

Let  $T$  be an interface element of the configuration shown in Fig. 2. Recall that the subelement  $T_1$  containing the vertex  $A_1$  and  $T_2$  contains  $A_8$ . Then we have the following stability estimates for  $C_T$ .

**Lemma 4.3.** On each interface element  $T$ , there holds

$$|C_T(p)|_{H^j(T_2)} \leq C|p|_{H^j(T_2)}, \quad j = 0, 1, \quad \forall p \in \mathbb{Q}_1, \quad (4.7a)$$

$$|C_T^{-1}(p)|_{H^j(T_2)} \leq C \frac{\beta^+}{\beta^-} |p|_{H^j(T_2)}, \quad j = 0, 1, \quad \forall p \in \mathbb{Q}_1, \quad (4.7b)$$

for the interface element types:

- Types I and II in Fig. 2;
- Type III in Fig. 2, if  $|A_4D_4| \geq \frac{1}{2}|A_4A_3|$  or  $|A_2D_1| \geq \frac{1}{2}|A_2A_1|$  or  $|A_6D_2| \geq \frac{1}{2}|A_6A_5|$  or  $|A_8D_3| \geq \frac{1}{2}|A_8A_7|$ ;
- Types IV and V in Fig. 2.

**Proof.** Also we only show the proof for the interface element of Type III in Fig. 2. First of all, we note that

$$|L|_{H^j(T_2)} \leq Ch^{1-j}|T_2|^{1/2} \leq Ch^{5/2-j}, \quad j = 0, 1. \quad (4.8)$$

Due to symmetry, we only need to consider the edge  $A_4A_3$ , namely assuming  $|A_4D_4| \geq \frac{1}{2}|A_4A_3|$  as shown in Fig. 4(a). We consider the tetrahedron  $A_4D_1D_3D_4$  denoted as  $P$ . Since  $|A_4D_4| \geq \frac{1}{2}|A_4A_3|$ , we know that  $|P| \geq h^3/12$ . Therefore, according to Lemma 4.2 and (4.8), we use (3.3a) to obtain

$$\begin{aligned} |C_T(p)|_{H^j(T_2)} &\leq |p|_{H^j(T_2)} + \max\left\{\frac{\beta^-}{\beta^+}, 1\right\} \|\nabla p(F)\| |L|_{H^j(T_2)} \\ &\leq |p|_{H^j(T_2)} + Ch^{1-j} \|\nabla p\|_{L^2(P)} \leq |p|_{H^j(T_2)} + C|p|_{H^j(P)} \end{aligned} \quad (4.9)$$

where in the last inequality we have also used the inverse inequality for  $j = 0$  on  $P$ . Furthermore, recalling that  $\tilde{T}_2$  is the subelement cut by the plane passing through  $D_1D_4D_3$ , and applying (4.2) to the last inequality in (4.9), we have

$$|C_T(p)|_{H^j(T_2)} \leq |p|_{H^j(T_2)} + C|p|_{H^j(\tilde{T}_2)} \leq |p|_{H^j(T_2)} + C|p|_{H^j(T_2)}, \quad (4.10)$$

which gives (4.7a). For (4.7b), similar to (4.9) and (4.10), we use (3.3b) to obtain

$$|\mathcal{C}_T^{-1}(p)|_{H^j(T_2)} \leq |p|_{H^j(T_2)} + \max\left\{\frac{\beta^+}{\beta^-}, 1\right\} \|\nabla p(F)\| |L|_{H^j(T_2)} \leq |p|_{H^j(T_2)} + C \frac{\beta^+}{\beta^-} |p|_{H^j(P)} \leq C \frac{\beta^+}{\beta^-} |p|_{H^j(T_2)}. \quad (4.11)$$

This finishes the proof.  $\square$

**Lemma 4.4.** *On each interface element  $T$ , there holds*

$$|\mathcal{C}_T(p)|_{H^j(T_1)} \leq C |p|_{H^j(T_1)}, \quad j = 0, 1, \quad \forall p \in \mathbb{Q}_1, \quad (4.12a)$$

$$|\mathcal{C}_T^{-1}(p)|_{H^j(T_1)} \leq C \frac{\beta^+}{\beta^-} |p|_{H^j(T_1)}, \quad j = 0, 1, \quad \forall p \in \mathbb{Q}_1, \quad (4.12b)$$

for the interface element types

- Type III in Fig. 2, if  $|A_4D_4| \leq \frac{1}{2}|A_4A_3|$  or  $|A_2D_1| \leq \frac{1}{2}|A_2A_1|$  or  $|A_6D_2| \leq \frac{1}{2}|A_6A_5|$  or  $|A_8D_3| \leq \frac{1}{2}|A_8A_7|$ ;
- Type V in Fig. 2.

**Proof.** We still only consider the interface element of Type III and the edge  $A_4A_3$ , and without loss of generality we assume  $|A_4D_4| \leq \frac{1}{2}|A_4A_3|$ , i.e.,  $|A_3D_4| \geq |A_4A_3|/2$  as shown in Fig. 4(b). In this case, we consider the tetrahedron  $P = A_3D_1D_4D_3$  and by a similar discussion, we also have  $|P| \geq h^3/12$ . Therefore, similar to (4.9), we have

$$\begin{aligned} |\mathcal{C}_T(p)|_{H^j(T_1)} &\leq |p|_{H^j(T_1)} + \max\left\{\frac{\beta^-}{\beta^+}, 1\right\} \|\nabla p(F)\| |L|_{H^j(T_1)} \\ &\leq |p|_{H^j(T_1)} + Ch^{1-j} \|\nabla p\|_{L^2(P)} \leq |p|_{H^j(T_1)} + C |p|_{H^j(P)} \end{aligned} \quad (4.13)$$

where in the last inequality we also use the inverse inequality for  $j = 0$  on  $P$ . Finally, similar to (4.10) but applying (4.1) to bound the last term in (4.13), we have (4.12a). (4.12b) can be proved by a similar argument.  $\square$

The estimates above can be understood as the stability of the extension operator  $\mathcal{C}_T$  for polynomials, and they serve as the foundation of the stability of the PPIFE method, namely, the inverse and trace inequalities. Now we are ready to present those inequalities for the proposed IFE functions.

**Theorem 4.5 (Trace inequalities).** *On each interface element  $T$  and its face  $F$ , one of the following must hold for all  $\phi_T \in S_h(T)$*

$$\|\nabla \phi_T \cdot \mathbf{n}\|_{L^2(F)} \leq Ch^{-1/2} \|\nabla \phi_T\|_{L^2(T)}, \quad (4.14a)$$

$$\|\beta \nabla \phi_T \cdot \mathbf{n}\|_{L^2(F)} \leq Ch^{-1/2} \|\beta \nabla \phi_T\|_{L^2(T)}. \quad (4.14b)$$

**Proof.** We only present the detailed proof for the interface element of Type III in Fig. 2. Due to the symmetry, we can assume the subelement containing  $A_1$  is  $T^-$ , i.e.,  $T_1 = T^-$ , and then the subelement containing  $A_8$  is  $T^+$ , i.e.,  $T_2 = T^+$ . Furthermore, without loss of generality, we only consider the interface face  $F = A_1A_2A_3A_4$ . Here we note that  $F^s = F \cap T^s$ ,  $s = \pm$ , are all curved-edge quadrilaterals. According to the definition (3.4), for each IFE function  $\phi_T$ , there exists a polynomial  $p \in \mathbb{Q}_1$  such that  $\phi_T = \phi_T^- = p$  on  $T^-$  and  $\phi_T = \phi_T^+ = \mathcal{C}_T(p)$  on  $T^+$ .

On one hand, we first consider the case  $|A_4D_4| \geq \frac{1}{2}|A_4A_3|$ . On  $T^+$ , we simply apply the standard trace inequality [50] on the whole element  $T$  to obtain

$$\begin{aligned} \|\beta^+ \nabla \phi_T \cdot \mathbf{n}\|_{L^2(F^+)} &= \|\beta^+ \nabla \mathcal{C}_T(p) \cdot \mathbf{n}\|_{L^2(F^+)} \leq \|\beta^+ \nabla \mathcal{C}_T(p) \cdot \mathbf{n}\|_{L^2(F)} \\ &\leq Ch^{-1/2} |\beta^+ \mathcal{C}_T(p)|_{H^1(T)} \leq Ch^{-1/2} |\beta^+ \mathcal{C}_T(p)|_{H^1(T^+)} \end{aligned} \quad (4.15)$$

where in the last inequality we have used (4.2). Similarly, applying the standard trace inequality [50] on the whole element  $T$  with (4.12b), we have

$$\begin{aligned} \|\nabla \phi_T \cdot \mathbf{n}\|_{L^2(F^-)} &= \|\nabla p \cdot \mathbf{n}\|_{L^2(F^-)} \leq \|\nabla p \cdot \mathbf{n}\|_{L^2(F)} \leq Ch^{-1/2} |p|_{H^1(T)} \\ &\leq Ch^{-1/2} \left( |\mathcal{C}_T^{-1}(\mathcal{C}_T(p))|_{H^1(T^+)} + |p|_{H^1(T^-)} \right) \leq Ch^{-1/2} \left( \frac{\beta^+}{\beta^-} |\mathcal{C}_T(p)|_{H^1(T^+)} + |p|_{H^1(T^-)} \right). \end{aligned} \quad (4.16)$$

Combining (4.15) and (4.16), we have the desired result (4.14b).

On the other hand, if  $|A_4D_4| \leq \frac{1}{2}|A_4A_3|$ , we apply the argument (4.15) to  $\nabla \phi_T \cdot \mathbf{n}$  on  $T^-$  with (4.1) to obtain

$$\|\nabla \phi_T \cdot \mathbf{n}\|_{L^2(F^-)} = \|\nabla p \cdot \mathbf{n}\|_{L^2(F^-)} \leq \|\nabla p \cdot \mathbf{n}\|_{L^2(F)} \leq Ch^{-1/2} |p|_{H^1(T)} \leq Ch^{-1/2} |p|_{H^1(T^-)}. \quad (4.17)$$

In addition, we apply the argument (4.16) to  $\nabla \phi_T \cdot \mathbf{n}$  on  $T^+$  with (4.7a) to obtain

$$\begin{aligned} \|\nabla\phi_T \cdot \mathbf{n}\|_{L^2(F^+)} &= \|\nabla C_T(p) \cdot \mathbf{n}\|_{L^2(F^+)} \leq \|\nabla C_T(p) \cdot \mathbf{n}\|_{L^2(F)} \leq Ch^{-1/2} |C_T(p)|_{H^1(T)} \\ &\leq Ch^{-1/2} (|C_T(p)|_{H^1(T^+)} + |C_T(p)|_{H^1(T^-)}) \leq Ch^{-1/2} (|C_T(p)|_{H^1(T^+)} + |p|_{H^1(T^-)}) \leq Ch^{-1/2} |\phi_T|_{H^1(T)}. \end{aligned} \tag{4.18}$$

Finally, combining (4.17) and (4.18), we have (4.14a)  $\square$

**Remark 4.6.** Roughly speaking, for each interface element  $T$ , if the size of the subelement corresponding to the larger coefficient  $\beta^+$  shrinks to 0, then the trace inequality (4.14b) holds. On the other hand, if the subelement corresponding to the smaller coefficient  $\beta^-$  shrinks, then (4.14a) holds. These two inequalities can be unified as the following one

$$\|\beta \nabla\phi_T \cdot \mathbf{n}\|_{L^2(F)} \leq Ch^{-1/2} \frac{\beta^+}{\sqrt{\beta^-}} \|\sqrt{\beta} \nabla\phi\|_{L^2(T)}. \tag{4.19}$$

In addition, we note that the IFE functions on interface elements may not be continuous across the interface. Here we present a special type of trace inequality for IFE functions which shows the difference between the two polynomial components on interface can be bounded by the IFE function on the element with certain optimal order of  $h$ . This is important to estimate the inconsistency error. For this purpose, let us first estimate  $L(X) = (X - F) \cdot \mathbf{n}$  on  $\Gamma \cap T$ .

**Lemma 4.7.** For each interface element  $T$ , there holds

$$\|L\|_{L^2(\Gamma \cap T)} \leq Ch^3. \tag{4.20}$$

**Proof.** For each  $X \in \Gamma \cap T$ , we denote the projection of  $X$  onto the approximate plane  $\tau_T$  by  $X_\perp$ . Using (2.4a), the fact  $L(X) = 0$  for every  $X \in \tau_T$ , and Lemma 2.3 we have

$$\|L\|_{L^2(\Gamma \cap T)} = \left( \int_{\Gamma \cap T} ((X - F) \cdot \mathbf{n})^2 dS \right)^{1/2} = \left( \int_{\Gamma \cap T} ((X - X_\perp) \cdot \mathbf{n})^2 dS \right)^{1/2} \leq C \|X - X_\perp\| |\Gamma \cap T|^{1/2} \leq Ch^3. \quad \square \tag{4.21}$$

Now, let us define  $[p]$  as the difference between one polynomial  $p$  and its image  $C_T(p)$ , namely  $[p] := C_T(p) - p$ . In particular,  $[\phi_T] = \phi_T^+ - \phi_T^-$ . As it is a polynomial,  $[p]$  is well-defined everywhere over the whole element. When it is restricted onto  $\Gamma \cap T$ , it is the same as  $[\![\cdot]\!]$ .

**Theorem 4.8.** For each interface element  $T$ , there holds

$$\|[\phi_T]\|_{L^2(T \cap \Gamma)} \leq C \frac{\sqrt{\beta^+}}{\beta^-} h^{3/2} \|\sqrt{\beta} \nabla\phi_T\|_{L^2(T)}, \quad \forall \phi_T \in S_h(T). \tag{4.22}$$

**Proof.** We only consider the interface element of Type III shown in Fig. 2(c), and without loss of generality we assume that the subelement  $T_1$  containing  $A_1$  is  $T^-$ , i.e.,  $T_1 = T^-$ , and then the subelement  $T_2$  containing  $A_8$  is  $T^+$ , i.e.,  $T_2 = T^+$ . According to the relation  $C_T$  between the two polynomial components of an IFE function (3.3), we note that there exists a polynomial  $p \in \mathbb{Q}_1$  such that  $\phi_T^+ = C_T(p)$ ,  $\phi_T^- = p$  and

$$[\phi_T] = \left( \frac{\beta^-}{\beta^+} - 1 \right) (\nabla p(F) \cdot \mathbf{n}) L = \left( \frac{\beta^+}{\beta^-} - 1 \right) (\nabla C_T(p)(F) \cdot \mathbf{n}) L. \tag{4.23}$$

If  $|A_4 D_4| \geq \frac{1}{2} |A_4 A_3|$ , using the similar argument to (4.9) and (4.10) with Lemma 4.2 on the tetrahedron  $A_4 D_1 D_4 D_3$  as shown in Fig. 4(a), we have  $|\nabla C_T(p)(F) \cdot \mathbf{n}| \leq Ch^{-3/2} \|\nabla C_T(p)\|_{L^2(T^+)}$ . Then we use the second equality in (4.23) and Lemma 4.7 to obtain

$$\begin{aligned} \|[\phi_T]\|_{L^2(\Gamma \cap T)} &\leq C \frac{\beta^+}{\beta^-} |\nabla C_T(p)(F) \cdot \mathbf{n}| \|L\|_{L^2(\Gamma \cap T)} \\ &\leq C \frac{\beta^+}{\beta^-} h^{3/2} \|\nabla C_T(p)\|_{L^2(T^+)} \leq C \frac{\sqrt{\beta^+}}{\beta^-} h^{3/2} \|\sqrt{\beta} \nabla\phi_T\|_{L^2(T)}. \end{aligned} \tag{4.24}$$

If  $|A_4 D_4| \leq \frac{1}{2} |A_4 A_3|$ , using the similar argument to (4.13) with Lemma 4.2 on the tetrahedron  $A_3 D_1 D_4 D_3$  as shown in Fig. 4(b), we have

$$|\nabla p(F) \cdot \mathbf{n}| \leq Ch^{-3/2} \|\nabla p\|_{L^2(T^-)}.$$

Then we apply the first equality in (4.23) and Lemma 4.7 to obtain

$$\|[\phi_T]\|_{L^2(\Gamma \cap T)} \leq C \frac{\beta^-}{\beta^+} |\nabla p(F) \cdot \bar{\mathbf{n}}| \|L\|_{L^2(\Gamma \cap T)} \leq C \frac{\sqrt{\beta^-}}{\beta^+} h^{3/2} \|\sqrt{\beta^-} \nabla p\|_{L^2(T^-)} \leq C \frac{\sqrt{\beta^-}}{\beta^+} h^{3/2} \|\sqrt{\beta} \nabla \phi_T\|_{L^2(T)}. \quad (4.25)$$

Combining (4.24) and (4.25) and noticing that  $\frac{\sqrt{\beta^-}}{\beta^+} \leq \frac{\sqrt{\beta^+}}{\beta^-}$ , we have finished the proof.  $\square$

**Theorem 4.9.** For each interface element  $T$ , there holds

$$\|[\phi_T]\|_{L^2(T \cap \Gamma)} \leq Ch^2 \|\llbracket \nabla \phi_T \rrbracket\|_{L^2(T \cap \Gamma)}, \quad \forall \phi_T \in S_h(T). \quad (4.26)$$

**Proof.** For simplicity, we denote  $w = [\phi_T]$  and note that  $w = 0$  on the approximate plane  $\tau_T$ . For each  $X \in \Gamma \cap T$ , let  $X_\perp$  be the projection of  $X$  onto  $\tau_T$ . Then the Taylor expansion yields

$$0 = w(X_\perp) = w(X) + \partial_\zeta w(X) |X - X_\perp| + \partial_\zeta^2 w(X) |X - X_\perp|^2 + \partial_\zeta^3 w(X) |X - X_\perp|^3 \quad (4.27)$$

where  $\zeta$  is the directional vector from  $X_\perp$  to  $X$ . Hence using (2.4a) and the fact that  $w$  is a linear polynomial, we have  $\partial_\zeta w = \partial_\zeta^2 w = 0$ . Then, (4.26) follows from taking integration over  $T \cap \Gamma$ .  $\square$

**Theorem 4.10 (Inverse inequalities).** For each interface element  $T$ , there holds

$$\|\nabla \phi_T\|_{L^2(T)} \leq C \frac{\beta^+}{\beta^-} h^{-1} \|\phi\|_{L^2(T)}, \quad \forall \phi_T \in S_h(T). \quad (4.28)$$

**Proof.** Following the convention above, we again only discuss the interface element of Type III shown in Fig. 2(c). Without loss of generality we assume that the subelement  $T_1$  containing  $A_1$  is  $T^-$  while the subelement  $T_2$  containing  $A_8$  is  $T^+$ . Recall that there is a polynomial  $p \in \mathbb{Q}_1$ ,  $\phi_T^- = p$  and  $\phi_T^+ = C_T(p)$ . The argument is actually similar to the one for Theorem 4.5.

First, if  $|A_4 D_4| \geq \frac{1}{2} |A_4 A_3|$ , then for  $\nabla \phi_T$  on  $T^+$ , we apply the standard inverse inequality with (4.2) to obtain

$$\|\nabla \phi_T\|_{L^2(T^+)} = \|\nabla C_T(p)\|_{L^2(T^+)} \leq \|\nabla C_T(p)\|_{L^2(T)} \leq Ch^{-1} \|C_T(p)\|_{L^2(T)} \leq Ch^{-1} \|C_T(p)\|_{L^2(T^+)}. \quad (4.29)$$

For  $\nabla \phi_T$  on  $T^-$ , we apply the standard inverse inequality and (4.7b) to have

$$\begin{aligned} \|\nabla \phi_T\|_{L^2(T^-)} &\leq \|\nabla p\|_{L^2(T)} \leq Ch^{-1} \|p\|_{L^2(T)} \leq Ch^{-1} (\|p\|_{L^2(T^-)} + \|p\|_{L^2(T^+)}) \\ &= Ch^{-1} \left( \|p\|_{L^2(T^-)} + \|C_T^{-1}(C_T(p))\|_{L^2(T^+)} \right) \leq Ch^{-1} \left( \|p\|_{L^2(T^-)} + \frac{\beta^+}{\beta^-} \|C_T(p)\|_{L^2(T^+)} \right). \end{aligned} \quad (4.30)$$

Combining (4.29) and (4.30), we have (4.28).

Second, if  $|A_4 D_4| \leq \frac{1}{2} |A_4 A_3|$ , then for  $\nabla \phi_T$  on  $T^+$ , applying the argument in (4.30) but with (4.12a), we obtain

$$\begin{aligned} \|\nabla \phi_T\|_{L^2(T^+)} &= \|C_T(p)\|_{L^2(T^+)} \leq \|\nabla C_T(p)\|_{L^2(T)} \leq Ch^{-1} \|C_T(p)\|_{L^2(T)} \\ &\leq Ch^{-1} (\|C_T(p)\|_{L^2(T^-)} + \|C_T(p)\|_{L^2(T^+)}) \leq Ch^{-1} (\|p\|_{L^2(T^-)} + \|C_T(p)\|_{L^2(T^+)}). \end{aligned} \quad (4.31)$$

In addition, for  $\nabla \phi_T$  on  $T^-$ , applying the argument in (4.29) but with (4.1), we have

$$\|\nabla \phi_T\|_{L^2(T^-)} = \|\nabla p\|_{L^2(T^-)} \leq \|\nabla p\|_{L^2(T)} \leq Ch^{-1} \|p\|_{L^2(T)} \leq Ch^{-1} \|p\|_{L^2(T^-)}. \quad (4.32)$$

Combining (4.31) and (4.32), we finish the proof.  $\square$

### 5. Error estimates of IFE solutions

In this section, we proceed to estimate the errors of the PPIFE scheme (3.9). For this purpose, we define the energy norm:

$$\|v\|^2 := \sum_{T \in \mathcal{T}_h} \|\sqrt{\beta} \nabla v\|_{L^2(T)}^2 + \sum_{F \in \mathcal{F}_h^i} \sigma \|h^{-1/2} \llbracket v \rrbracket\|_{L^2(F)}^2 + \sum_{F \in \mathcal{F}_h^i} \frac{1}{\sigma} \|h^{1/2} \{\beta \nabla v \cdot \mathbf{n}\}\|_{L^2(F)}^2. \quad (5.1)$$

It is easy to see that  $\|\cdot\|$  is a semi-norm. We begin by showing that the functional above is indeed a norm on the space  $V_h(\Omega)$ .

**Lemma 5.1.**  $\|\cdot\|$  is a norm of  $V_h(\Omega)$ .

**Proof.** Since  $\|v\|^2 = 0$ , we directly have  $\|\nabla v\| = 0$ , and thus  $v$  is a constant on each element. Due to the continuity at mesh nodes and zero trace on  $\partial\Omega$ , we know that  $v$  must be zero on the whole domain.  $\square$

Now we show that the bilinear form  $a_h(\cdot, \cdot)$  is both continuous and coercive under the energy norm  $\|\cdot\|$ .

**Theorem 5.2.** *There exists a constant  $C$  such that*

$$a_h(v, w) \leq C \|v\| \|w\|, \quad \forall v, w \in V_h(\Omega). \tag{5.2}$$

**Proof.** It directly follows from the Hölder's inequality.  $\square$

**Theorem 5.3.** *Assume that  $\sigma$  is large enough, then there holds*

$$a_h(v, v) \geq \frac{1}{4} \|v\|^2, \quad \forall v \in S_h(\Omega). \tag{5.3}$$

**Proof.** We first note that

$$a_h(v, v) = \sum_{T \in \mathcal{T}_h} \|\sqrt{\beta} \nabla v\|_{L^2(T)}^2 + (\epsilon - 1) \sum_{F \in \mathcal{F}_h^i} \int_F \{\beta \nabla v \cdot \mathbf{n}\} [v] dS + \sum_{F \in \mathcal{F}_h^i} \frac{\sigma}{h} \|[v]\|_{L^2(F)}^2 dS. \tag{5.4}$$

Then we only need to bound the second term in (5.4). On each interface face  $F$ , we denote its two neighbor elements by  $T_F^1$  and  $T_F^2$ . Then we apply (4.19) to obtain

$$\|\{\beta \nabla v \cdot \mathbf{n}\}\|_{L^2(F)} \leq \frac{1}{2} \sum_{j=1,2} \|\beta \nabla v|_{T_F^j} \cdot \mathbf{n}\|_{L^2(F)} \leq C \frac{\beta^+}{2\sqrt{\beta^-}} \sum_{j=1,2} h^{-1/2} \|\sqrt{\beta} \nabla v\|_{L^2(T_F^j)}. \tag{5.5}$$

Using Hölder's inequality and Young's inequality, we have

$$\begin{aligned} \left| (\epsilon - 1) \int_F \{\beta \nabla v \cdot \mathbf{n}\} [v] dS \right| &\leq 2 \left( h^{1/2} \|\{\beta \nabla v \cdot \mathbf{n}\}\|_{L^2(F)} \right) \left( h^{-1/2} \|[v]\|_{L^2(F)} \right) \\ &\leq \left( \sum_{j=1,2} \|\sqrt{\beta} \nabla v\|_{L^2(T_F^j)} \right) \left( h^{-1/2} C \frac{\beta^+}{\sqrt{\beta^-}} \|[v]\|_{L^2(F)} \right) \\ &\leq \frac{1}{12} \left( \sum_{j=1,2} \|\sqrt{\beta} \nabla v\|_{L^2(T_F^j)}^2 \right) + 6 \left( C^2 \frac{(\beta^+)^2}{\beta^- h} \|[v]\|_{L^2(F)}^2 \right). \end{aligned} \tag{5.6}$$

Summing (5.6) over all the interface faces, we have

$$\left| (\epsilon - 1) \sum_{F \in \mathcal{F}_h^i} \int_F \{\beta \nabla v \cdot \mathbf{n}\} [v] dS \right| \leq \frac{1}{2} \sum_{T \in \mathcal{T}_h} \|\sqrt{\beta} \nabla v\|_{L^2(T)}^2 + 6C^2 \frac{(\beta^+)^2 / \beta^-}{h} \sum_{F \in \mathcal{F}_h^i} \|[v]\|_{L^2(F)}^2. \tag{5.7}$$

Similarly, using (4.19) again, we have

$$\sum_{F \in \mathcal{F}_h^i} \|h^{1/2} \{\beta \nabla v \cdot \mathbf{n}\}\|_{L^2(F)}^2 \leq 3 \sum_{T \in \mathcal{T}_h} C^2 \frac{(\beta^+)^2}{\beta^-} \|\sqrt{\beta} \nabla v\|_{L^2(T)}^2. \tag{5.8}$$

Taking  $\sigma = 12C^2 \frac{(\beta^+)^2}{\beta^-}$  and putting (5.7) and (5.8) into (5.4), we have

$$\begin{aligned} a_h(v, v) &\geq \sum_{T \in \mathcal{T}_h} \left( 1 - \frac{1}{2} - \frac{1}{4} \right) \|\sqrt{\beta} \nabla v\|_{L^2(T)}^2 + \left( \sigma - 6C^2 \frac{(\beta^+)^2}{\beta^-} \right) h^{-1} \sum_{F \in \mathcal{F}_h^i} \|[v]\|_{L^2(F)}^2 \\ &\quad + \sum_{F \in \mathcal{F}_h^i} (\sigma)^{-1} \|h^{1/2} \{\beta \nabla v \cdot \mathbf{n}\}\|_{L^2(F)}^2 \geq \frac{1}{4} \|v\|^2. \quad \square \end{aligned} \tag{5.9}$$

Let  $u_E^s \in H_0^2(\Omega)$  be the Sobolev extension of  $u^s = u|_{\Omega^s}$  from  $\Omega^s$  to  $\Omega$ ,  $s = \pm$ . According to the boundedness of Sobolev extensions Theorem 7.25 in [16] and Poincaré inequality, there holds

$$|u_E^s|_{H^1(\Omega)} + |u_E^s|_{H^2(\Omega)} \leq C_E(|u^s|_{H^1(\Omega^s)} + |u^s|_{H^2(\Omega^s)}), \quad s = \pm, \tag{5.10}$$

for some constant  $C_E$  only depending on  $\Omega^\pm$ . Now we recall the nodal interpolation  $\mathcal{I}_h$  for IFE functions from [20]:

$$\mathcal{I}_h : H^2(\Omega^+ \cup \Omega^-) \rightarrow S_h(\Omega), \quad \mathcal{I}_h u(X) = u(X), \quad \forall X \in \mathcal{N}_h. \tag{5.11}$$

According to Theorem 4.3 from [20], if  $u$  satisfies the jump conditions,  $\mathcal{I}_h u - u$  has the optimal convergence rate with respect to the mesh size  $h$  on each patch  $\omega_T$  defined in (2.3) of an interface element  $T$ , namely,

$$|u - \mathcal{I}_h u|_{H^k(\omega_T)} \leq C \frac{\beta^+}{\beta^-} h^{2-k} \sum_{j=1,2} (|u_E^+|_{H^j(\omega_T)} + |u_E^-|_{H^j(\omega_T)}), \quad k = 0, 1, 2. \tag{5.12}$$

We can further use this result to estimate the interpolation errors in terms of the energy norm.

**Lemma 5.4.** Assume that the mesh  $\mathcal{T}_h$  is fine enough, then we have

$$\|u - \mathcal{I}_h u\| \leq C \frac{(\beta^+)^2}{(\beta^-)^{3/2}} h \sum_{j=1,2} (|u^+|_{H^j(\Omega^+)} + |u^-|_{H^j(\Omega^-)}). \tag{5.13}$$

**Proof.** First of all, (5.12) and the standard estimate of the Lagrange interpolation for finite element functions give

$$\|\sqrt{\beta} \nabla(u - \mathcal{I}_h u)\|_{L^2(T)} \leq C \frac{(\beta^+)^{3/2}}{\beta^-} h \sum_{s=\pm} (|u_E^s|_{H^1(\omega_T)} + |u_E^s|_{H^2(\omega_T)}). \tag{5.14}$$

For the second term in (5.1), for each  $F \in \mathcal{F}_h^i$ , we denote  $T_F^1$  and  $T_F^2$  as the two neighbor elements. Using the trace inequality and (5.12), we have

$$\begin{aligned} \sqrt{\sigma} \|h^{-1/2} [u - \mathcal{I}_h u]\|_{L^2(F)} &\leq C \frac{\beta^+}{(\beta^-)^{1/2}} \sum_{r=1,2} (h^{-1} \|u - \mathcal{I}_h u\|_{L^2(T_F^r)} + |u - \mathcal{I}_h u|_{H^1(T_F^r)}) \\ &\leq C \frac{(\beta^+)^2}{(\beta^-)^{3/2}} h \sum_{r=1,2} \sum_{s=\pm} (|u_E^s|_{H^1(\omega_{T_F^r})} + |u_E^s|_{H^2(\omega_{T_F^r})}). \end{aligned} \tag{5.15}$$

For the third term in (5.1), by similar derivation we have

$$\frac{1}{\sqrt{\sigma}} \|h^{1/2} \{\beta \nabla(u - \mathcal{I}_h u) \cdot \mathbf{n}\}\|_{L^2(F)} \leq C \frac{\beta^+}{(\beta^-)^{1/2}} h \sum_{r=1,2} \sum_{s=\pm} (|u_E^s|_{H^1(\omega_{T_F^r})} + |u_E^s|_{H^2(\omega_{T_F^r})}). \tag{5.16}$$

Summing the estimates above over all the elements and interface faces, using the finite overlapping of the patches  $\omega_T$ ,  $T \in \mathcal{T}_h^i$ , and applying the boundedness (5.10), we have the desired result.  $\square$

Now we are ready to present the error estimates of IFE solutions in terms of the energy norm and  $L^2$  norm. We note that the key difficulty for these two estimates is the treatment of the non-consistence of the IFE scheme.

**Theorem 5.5.** Assume that the mesh  $\mathcal{T}_h$  is fine enough, and assume that  $\sigma$  is large enough such that Theorem 5.3 holds, then there holds

$$\|u - u_h\| \leq Ch \frac{(\beta^+)^2}{(\beta^-)^{5/2}} \sum_{j=1,2} (|\beta^- u^-|_{H^j(\Omega^-)} + |\beta^+ u^+|_{H^j(\Omega^+)}). \tag{5.17}$$

**Proof.** Let us first estimate the bound of  $b_h(u, v_h)$  for each  $v_h \in S_h(\Omega)$ . Using Theorem 4.8 and the trace inequality (Lemma 3.2 in [49]), we have

$$\begin{aligned}
 |b_h(u, v_h)| &\leq \sum_{T \in \mathcal{T}_h^i} \|\beta^- \nabla u^- \cdot \mathbf{n}\|_{L^2(\Gamma \cap T)} \| \llbracket v_h \rrbracket \|_{L^2(\Gamma \cap T)} \\
 &\leq C \frac{\sqrt{\beta^+}}{\beta^-} \sum_{T \in \mathcal{T}_h^i} (h^{-1/2} |\beta^- u_E^-|_{H^1(T)} + h^{1/2} |\beta^- u_E^-|_{H^2(T)}) h^{3/2} \|\sqrt{\beta} \nabla v_h\|_{L^2(T)} \\
 &\leq C \frac{\sqrt{\beta^+}}{\beta^-} h (|\beta^- u_E^-|_{H^1(\Omega)} + |\beta^- u_E^-|_{H^2(\Omega)}) \|v_h\|.
 \end{aligned} \tag{5.18}$$

Now we consider the Lagrange interpolation operator  $\mathcal{I}_h$ , and by Lemma 3.1 we write

$$a_h(u_h - \mathcal{I}_h u, v_h) = a_h(u - \mathcal{I}_h u, v_h) - b_h(u, v_h). \tag{5.19}$$

Taking  $v_h = u_h - \mathcal{I}_h u \in S_h(\Omega)$  and applying coercivity in Theorem 5.3, the boundedness in Theorem 5.2 as well as (5.18), we arrive at

$$\|u_h - \mathcal{I}_h u\|^2 \leq C \|u_h - \mathcal{I}_h u\| \|u - \mathcal{I}_h u\| + C \frac{\sqrt{\beta^+}}{\beta^-} h (|\beta^- u_E^-|_{H^1(\Omega)} + |\beta^- u_E^-|_{H^2(\Omega)}) \|u_h - \mathcal{I}_h u\|. \tag{5.20}$$

By the optimal approximation of  $\mathcal{I}_h u$  given in Lemma 5.4, (5.20) yields

$$\|u_h - \mathcal{I}_h u\| \leq C \frac{(\beta^+)^3}{(\beta^-)^{3/2}} h \sum_{j=1,2} (|u_E^-|_{H^j(\Omega)} + |u_E^+|_{H^j(\Omega)}) + C \frac{\sqrt{\beta^+}}{\beta^-} h (|\beta^- u_E^-|_{H^1(\Omega)} + |\beta^- u_E^-|_{H^2(\Omega)}). \tag{5.21}$$

Clearly, the triangle inequality together with (5.21) and (5.10) yields the desired result.  $\square$

**Remark 5.6.** The regularity of elliptic interface problems [12,34] gives that

$$\sum_{j=1,2} (|\beta^- u^-|_{H^j(\Omega^-)} + |\beta^+ u^+|_{H^j(\Omega^+)}) \leq C_{reg} \|f\|_{L^2(\Omega)}, \tag{5.22}$$

where the constant  $C_{reg}$  only depends on the  $\Omega^\pm$ . Thus, Theorem 5.5 yields

$$\|u - u_h\| \leq Ch \frac{(\beta^+)^2}{(\beta^-)^{5/2}} \|f\|_{L^2(\Omega)}. \tag{5.23}$$

**Theorem 5.7.** Under the conditions of Theorem 5.5 and the elliptic regularity (5.22), there holds

$$\|u - u_h\|_{L^2(\Omega)} \leq Ch^2 \frac{(\beta^+)^4}{(\beta^-)^5} \|f\|_{L^2(\Omega)}. \tag{5.24}$$

**Proof.** We use the duality argument. Define an auxiliary function  $z \in PH^2(\Omega)$  to be the solution of interface problem (2.1) with the right hand side  $f$  replaced by  $u - u_h \in L^2(\Omega)$ . Again, we consider the Lagrange interpolation operator  $\mathcal{I}_h$  for IFE functions (5.11). Testing this auxiliary equation with  $u - u_h$  and using the similar derivation to Lemma 3.1, we have

$$\begin{aligned}
 \|u - u_h\|_{L^2(\Omega)}^2 &= a_h(z, u - u_h) - b_h(z, u - u_h) \\
 &= a_h(z - \mathcal{I}_h z, u - u_h) + b_h(u, \mathcal{I}_h z) - b_h(z, u - u_h)
 \end{aligned} \tag{5.25}$$

where in the second equality we have used the identity (3.12) again. Lemma 5.4 for  $z$  and (5.23) show that

$$\begin{aligned}
 a_h(z - \mathcal{I}_h z, u - u_h) &\leq C \|z - \mathcal{I}_h z\| \|u - u_h\| \\
 &\leq C \frac{(\beta^+)^4}{(\beta^-)^5} h^2 \sum_{j=1,2} (|\beta^+ z^+|_{H^j(\Omega^+)} + |\beta^- z^-|_{H^j(\Omega^-)}) \|f\|_{L^2(\Omega)} \leq C \frac{(\beta^+)^4}{(\beta^-)^5} h^2 \|u - u_h\|_{L^2(\Omega)} \|f\|_{L^2(\Omega)}.
 \end{aligned} \tag{5.26}$$

For the second term on the right side of (5.25), using Theorem 4.9, we obtain

$$\begin{aligned}
 |b_h(u, \mathcal{I}_h z)| &\leq Ch^2 \sum_{T \in \mathcal{T}_h^i} \|\beta^- \nabla u^- \cdot \mathbf{n}\|_{L^2(\Gamma \cap T)} \| \llbracket \nabla \mathcal{I}_h z \rrbracket \|_{L^2(\Gamma \cap T)} \leq Ch^2 \|\beta^- \nabla u^- \cdot \mathbf{n}\|_{L^2(\Gamma)} \| \llbracket \nabla \mathcal{I}_h z \rrbracket \|_{L^2(\Gamma)} \\
 &\leq Ch^2 \|\beta^- \nabla u^- \cdot \mathbf{n}\|_{L^2(\Gamma)} (\| \llbracket \nabla (\mathcal{I}_h z - z) \rrbracket \|_{L^2(\Gamma)} + \| \llbracket \nabla z \rrbracket \|_{L^2(\Gamma)}).
 \end{aligned} \tag{5.27}$$

Let  $z_E^\pm$  be the Sobolev extensions of  $z^\pm = z|_{\Omega^\pm}$  from  $\Omega^\pm$  to  $\Omega$ . By the trace inequality Lemma 3.2 in [49] and (5.12) on each interface element, we have

$$\begin{aligned} \|\llbracket \nabla(\mathcal{I}_h z - z) \rrbracket\|_{L^2(\Gamma)} &\leq \sum_{T \in \mathcal{T}_h^i} \sum_{s=\pm} C(h^{-1/2} |\mathcal{I}_h z_E^s - z_E^s|_{H^1(T)} + h^{1/2} |\mathcal{I}_h z_E^s - z_E^s|_{H^2(T)}) \\ &\leq C \frac{\beta^+}{(\beta^-)^2} h^{1/2} \sum_{j=1,2} (|\beta^+ z^+|_{H^j(\Omega^-)} + |\beta^- z^-|_{H^j(\Omega^+)}) \leq C \frac{\beta^+}{(\beta^-)^2} h^{1/2} \|u - u_h\|_{L^2(\Omega)} \end{aligned} \tag{5.28}$$

where in the second inequality we have used the boundedness for Sobolev extensions. In addition, by the trace inequality from  $\Gamma$  to  $\Omega^\pm$ , we have

$$\|\llbracket \nabla z \rrbracket\|_{L^2(\Gamma)} \leq C \frac{1}{\beta^-} \sum_{j=1,2} (|\beta^+ z^+|_{H^j(\Omega^-)} + |\beta^- z^-|_{H^j(\Omega^+)}) \leq C \frac{1}{\beta^-} \|u - u_h\|_{L^2(\Omega)}. \tag{5.29}$$

Putting (5.28) and (5.29) into (5.27) and applying the trace inequality to  $\nabla u^- \cdot \mathbf{n}$  from  $\Gamma$  to  $\Omega^-$ , we get

$$|b_h(u, \mathcal{I}_h z)| \leq C \frac{\beta^+}{(\beta^-)^2} h^2 (|\beta^- u_E^-|_{H^1(\Omega)} + |\beta^- u_E^-|_{H^2(\Omega)}) \|u - u_h\|_{L^2(\Omega)}. \tag{5.30}$$

For the third term in (5.25), we note that  $u$  is continuous which implies  $b_h(z, u - u_h) = -b_h(z, u_h)$ . Then, its estimation is similar to (5.27) but with Theorem 4.8:

$$\begin{aligned} |b_h(z, u_h)| &\leq Ch^{3/2} \frac{\sqrt{\beta^+}}{\beta^-} \sum_{T \in \mathcal{T}_h^i} \|\beta^- \nabla z^- \cdot \mathbf{n}\|_{L^2(\Gamma \cap T)} \|\sqrt{\beta} \nabla u_h\|_{L^2(T)} \\ &\leq Ch^{3/2} \frac{\sqrt{\beta^+}}{\beta^-} (|\beta^- z^-|_{H^1(\Omega^-)} + |\beta^- z^-|_{H^2(\Omega^-)}) \sum_{T \in \mathcal{T}_h^i} (\|\sqrt{\beta} \nabla(u_h - u)\|_{L^2(T)} + \|\sqrt{\beta} \nabla u\|_{L^2(T)}). \end{aligned} \tag{5.31}$$

The estimate of  $\|\sqrt{\beta} \nabla(u_h - u)\|_{L^2(\Gamma)}$  simply follows from Theorem 5.5 with the error bound  $h \frac{(\beta^+)^2}{(\beta^-)^{5/2}} \|f\|_{L^2(\Omega)}$ . As for the term  $\|\sqrt{\beta} \nabla u\|_{L^2(T)}$ , we note that it only appears on the interface elements and  $\cup_{T \in \mathcal{T}_h^i} T \subseteq S_\delta := \{X \in \Omega : \text{dist}(X, \Gamma) \leq \delta\}$  with  $\delta = \sqrt{3}h$  where  $\text{dist}(X, \Gamma)$  denotes the distance between  $X$  and  $\Gamma$ . Then, applying the  $\delta$ -strip argument, see Lemma 3.1 in [31], we have

$$\sum_{T \in \mathcal{T}_h^i} \|\sqrt{\beta} \nabla u\|_{L^2(T)} \leq C \sqrt{\delta} \|\sqrt{\beta} \nabla u\|_{H^1(\Omega)} \leq Ch^{1/2} \frac{1}{\sqrt{\beta^-}} \|\beta \nabla u\|_{H^1(\Omega)} \leq Ch^{1/2} \frac{1}{\sqrt{\beta^-}} \|f\|_{L^2(\Omega)}. \tag{5.32}$$

Putting (5.32) into (5.31) and using the elliptic regularity for  $z$ , we obtain the bound for  $b_h(z, u_h)$  which is  $Ch^2 \frac{(\beta^+)^{5/2}}{(\beta^-)^{7/2}}$ . Substituting it with (5.26) and (5.30) into (5.25), we have (5.24).  $\square$

**Remark 5.8.** We are able to specify how the error bound depends on the material property parameters  $\beta^\pm$  at each step throughout the analysis. But it is important to note that the dependence on  $\beta^\pm$  in the final estimates in Theorem 5.5, (5.23) and Theorem 5.7 is due to the limitation of our analysis approach, since we do not observe such a severe effect from  $\beta^\pm$  in computation. How to achieve the optimal error bound with respect to  $\beta^\pm$  is an interesting topic in our future research.

### 6. Numerical experiments

In this section, we report some numerical experiments to demonstrate the performance of our IFE method. In the first four examples, we present artificial interface problems where we know the analytical function of the interface surface and the exact solution. In particular, we compare the numerical performance of the proposed PPIFE scheme and the classical IFE scheme in Example 1 and Example 2. The classical IFE scheme is to find  $u_h \in S_h(\Omega)$  such that

$$\sum_{T \in \mathcal{T}_h} \int_T \beta \nabla u_h \cdot \nabla v_h \, dx = \int_\Omega f v_h \, dx, \quad \forall v_h \in S_h(\Omega), \tag{6.1}$$

where no penalty is added. In Example 3, we consider a more complicated interface shape and the effect of the maximum angle conditions in the computation. In Example 4, we study an example with a singular interface. In Example 5, we present a real-world interface model of which the interface has a dabbling-duck shape but only the cloud-point data are available.

**Example 1 (Plane interface: recovering exact solutions).** In the first example, we compare the performance of the PPIFE and the classic IFE methods when the exact solutions are contained in the IFE spaces. Let  $\Omega = (-1, 1)^3$  and consider a planar interface  $\Gamma = \{(x, y, z) \in \Omega : \gamma(x, y, z) = 0\}$  where

**Table 1**  
PPIFE errors and the convergence rates for linear solution.

N	PPIFE			IFE		
	$e_h^\infty$	$e_h^0$	$e_h^1$	$e_h^\infty$	$e_h^0$	$e_h^1$
10	5.50E-15	2.29E-15	1.74E-14	7.23E-3	3.07E-3	4.95E-2
20	1.92E-15	6.37E-16	8.93E-15	2.75E-3	1.03E-3	2.47E-2
30	5.33E-15	3.87E-15	1.75E-14	1.87E-3	4.93E-4	2.24E-2
40	3.11E-15	2.04E-15	1.73E-14	1.81E-3	5.65E-4	2.37E-2

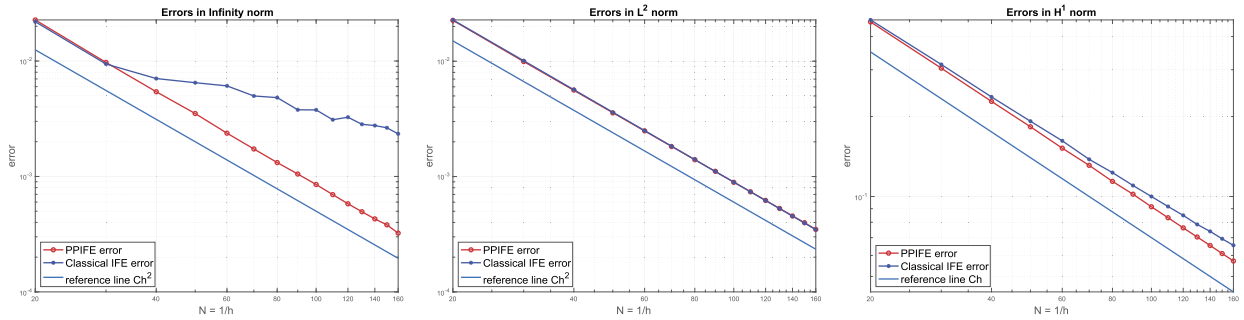


**Fig. 5.** Convergence in  $L^\infty$ ,  $L^2$ , and  $H^1$  norms of PPIFE and IFE solutions for Example 2.

$$\gamma(x, y, z) = \frac{1}{\sqrt{2}}(x + z - \pi/10).$$

Let the exact solution be

$$u(x, y, z) = \begin{cases} \frac{1}{\beta^-} \gamma(x, y, z) & \text{in } \Omega^- := \{(x, y, z) \in \Omega : \gamma(x, y, z) < 0\}, \\ \frac{1}{\beta^+} \gamma(x, y, z) & \text{in } \Omega^+ := \{(x, y, z) \in \Omega : \gamma(x, y, z) > 0\}. \end{cases} \tag{6.2}$$

Our computation is carried out on a family of uniform Cartesian meshes consisting of  $N^3$  cuboids. We report errors in the discrete  $L^\infty$ ,  $L^2$ , and  $H^1$ -norms, denoted by  $e_h^\infty$ ,  $e_h^0$ , and  $e_h^1$ , respectively. The errors for both PPIFE and IFE methods are reported in Table 1. We note that the PPIFE method actually recovers the exact solutions with no approximation errors (only round-off errors are observed). This suggests that PPIFE is a consistent numerical algorithm; namely, if the exact solution is a piecewise linear function separated by a planar interface, then the PPIFE method will reproduce the exact solution. In contrast, the classical IFE method without penalty cannot generate exact solution due to the inconsistency caused by the discontinuities of IFE functions across interface faces.

**Example 2 (Sphere interface).** In the second example, we let  $\Omega = (-1, 1)^3$  and let the interface be a sphere  $\Gamma = \{(x, y, z) : \gamma(x, y, z) = 0\}$  where  $\gamma(x, y, z) = x^2 + y^2 + z^2 - r^2$ . The exact solution is constructed as

$$u(x, y, z) = \begin{cases} -\cos\left(\frac{\pi(x^2 + y^2 + z^2)}{2r^2}\right) & \text{in } \Omega^- := \{(x, y, z) \in \Omega : \gamma(x, y, z) < 0\}, \\ x^2 + y^2 + z^2 - r^2 & \text{in } \Omega^+ := \{(x, y, z) \in \Omega : \gamma(x, y, z) > 0\}. \end{cases} \tag{6.3}$$

The parameters are chosen to be  $r = \pi/4$  and  $\beta^- = 1$ , and  $\beta^+ = \frac{\pi}{2r^2} \approx 2.5465$ . Our computation is carried out on a family of uniform Cartesian meshes consisting of  $N^3$  cuboids. We start from a coarse mesh with  $N = 20$  and stretch to a very fine mesh with  $N = 160$  by an increment of 10 more partitions in each direction for each finer mesh. We report errors in the discrete  $L^\infty$ ,  $L^2$ , and  $H^1$ -norms for both PPIFE and classical IFE methods. See Fig. 5 for a comparison of the performances in all three norms. Using linear regression, the errors of PPIFE solution obey

$$e_h^\infty \approx 9.898h^{2.034}, \quad e_h^0 \approx 9.093h^{2.004}, \quad e_h^1 \approx 9.017h^{0.999}.$$

Our numerical results show that the PPIFE method converges optimally in both  $L^2$  and  $H^1$  norms, which confirms our theoretical error bounds (5.17) and (5.24). We also observe that the convergence rate in  $L^\infty$  norm is also optimal for the PPIFE method, although we don't know how to theoretically prove it yet. The PPIFE method clearly outperforms the classical IFE method since their errors in  $L^\infty$  norm are much smaller than IFE method, and their convergence rates in  $L^2$  or  $H^1$  norm do not deteriorate as the mesh size becomes small. This is consistent with the observation for the 2D case [40]. For a more

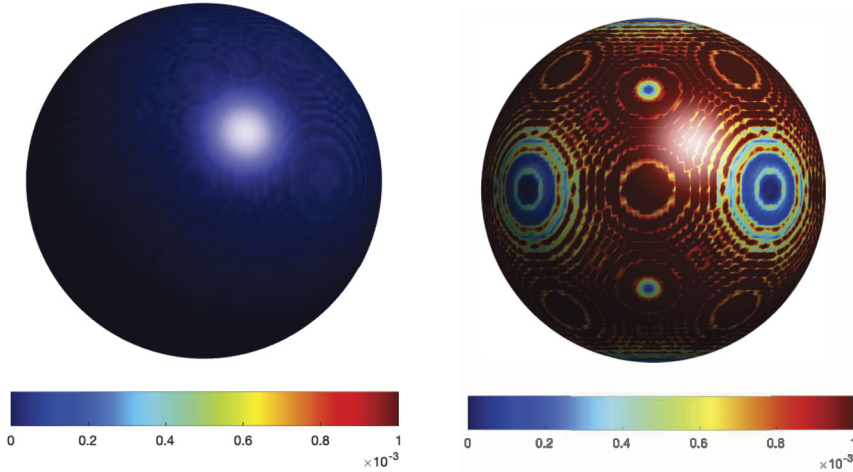


**Fig. 6.** A comparison of the PPIFE (left) and the classical IFE (right) errors on the interface surfaces for Example 2, (mesh size  $N = 100$ ). (For interpretation of the colors in the figure(s), the reader is referred to the web version of this article.)

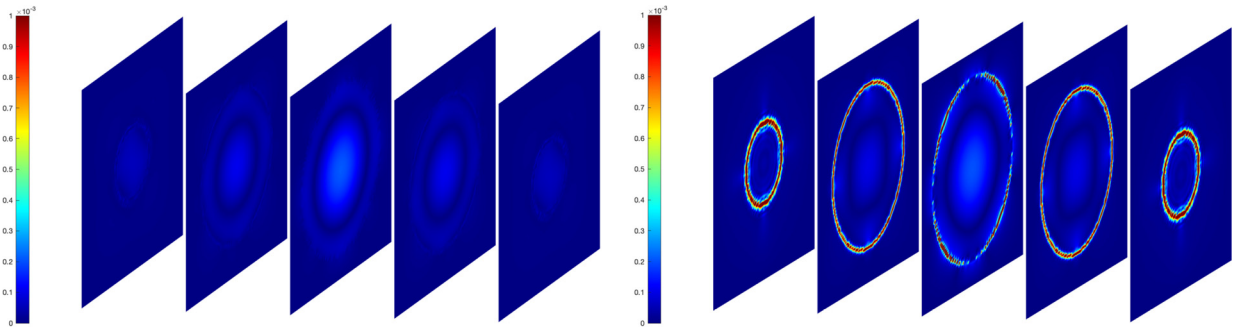


**Fig. 7.** A comparison of the PPIFE (left) and the classic IFE (right) errors on slices of the domain at  $y = -0.7, -0.35, 0, 0.35, \text{ and } 0.7$  for Example 2, (mesh size  $N = 100$ ).

visible comparison, we plot the errors of PPIFE and IFE methods on the interface surface itself in Fig. 6. Moreover, we plot the errors on five slices of the domain with  $y = -0.7, -0.35, 0, 0.35, \text{ and } 0.7$  in Fig. 7. From both of these figures, we can clearly see that the PPIFE errors around interface are significantly smaller and are comparable to the errors away from the interface. In contrary, the classical IFE solutions have much larger errors around the interface.

**Example 3 (More completed topology: an orthocircle interface).** In this example, we consider an interface problem with more complicated topology. We let  $\Omega = (-1.2, 1.2)^3$ , and let the interface be  $\Gamma = \{(x, y, z) \in \Omega : \gamma(x, y, z) = 0\}$  where

$$\gamma(x, y, z) = [(x^2 + y^2 - 1)^2 + z^2][(x^2 + z^2 - 1)^2 + y^2][(y^2 + z^2 - 1)^2 + x^2] - 0.075^2[1 + 3(x^2 + y^2 + z^2)].$$

The shape of the interface is plotted in the left plot of Fig. 8. This interface problem was reported in [10]. Let the exact solution be

$$u(x, y, z) = \begin{cases} \frac{1}{\beta^-} \gamma(x, y, z) & \text{in } \Omega^- := \{(x, y, z) \in \Omega : \gamma(x, y, z) < 0\}, \\ \frac{1}{\beta^+} \gamma(x, y, z) & \text{in } \Omega^+ := \{(x, y, z) \in \Omega : \gamma(x, y, z) > 0\}. \end{cases} \tag{6.4}$$

The coefficients are chosen to have a larger contrast as  $\beta^- = 1$  and  $\beta^+ = 100$ . The errors of the PPIFE method in all three norms are reported in Fig. 9. Again, we can see that overall convergence rates in  $L^2$  and  $H^1$  norms are close to optimal, which confirms our theoretical results. Using linear regression, the errors obey

$$e_h^\infty \approx 1.365h^{1.340}, \quad e_h^0 \approx 5.848h^{1.877}, \quad e_h^1 \approx 7.276h^{1.101}.$$

For comparison, we also report the solutions without imposing the maximum angle condition in Section 2. See the blue curves in Fig. 9. Although we can still see the convergence in all three norms, the magnitudes of errors are larger than the

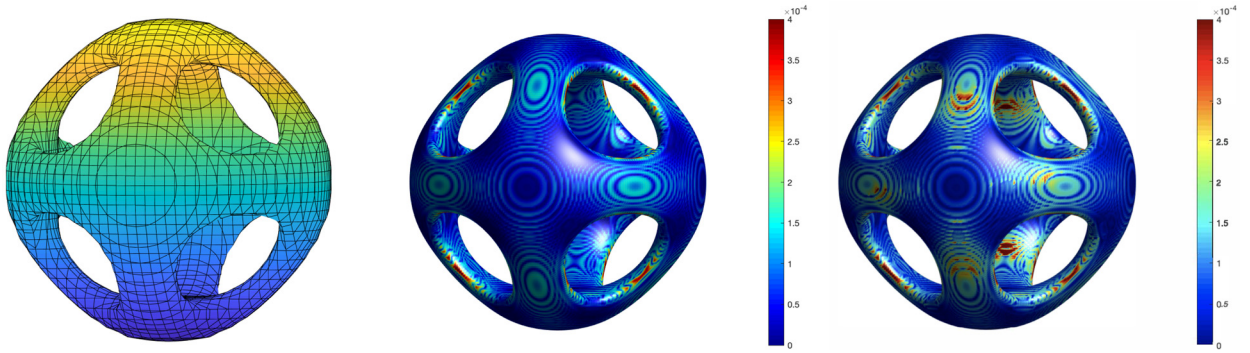


Fig. 8. A plot of the orthocircle interface (left). The error surfaces of PPIFE solutions with (middle) and without (right) imposing the maximal angle condition (mesh size  $N = 160$ ).

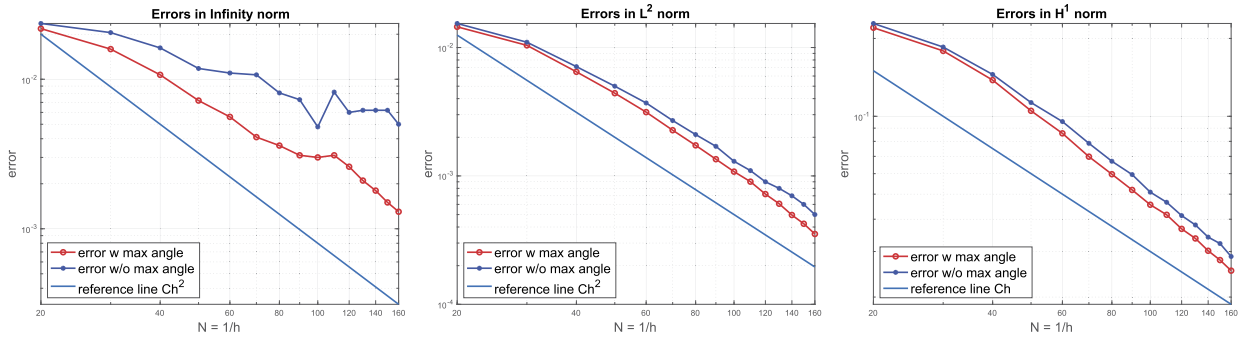


Fig. 9. Convergence of Example 3.

those enforced by the maximum angle condition, see the red curves in Fig. 9. We also compare the error surfaces of these two solutions on the interface. See the middle and right plots in Fig. 8. It can be observed that errors are larger on the interface when the maximal angle condition is not satisfied. These large errors are indicated by the red spots in the right plot in Fig. 8 which are also where the maximal conditions are violated.

Moreover, since the only extra work of the IFE method is to replace the standard shape functions by some special shape functions on interface elements, we report the percentage of interface elements over all elements, defined by  $|\mathcal{T}_h^i|/|\mathcal{T}_h|$ , for all three examples. The number of interface elements is expected to be  $\mathcal{O}(N^2)$ , and the number of all elements is  $\mathcal{O}(N^3)$ , so the percentage should be a linear function of the mesh size  $h = 1/N$ . In Fig. 10, we can observe this linear relationship clearly. Also, as the shape of interface elements becomes more complex from Example 1 to Example 3, the proportionality constant gets larger. However, even for complicated interface shapes, such as the orthocircle in Example 3, there are only less than 3% interface elements on our finest mesh ( $N = 160$ , around 4 million cuboids). As a result, the majority of the computation (over 97% of the total elements) can be done using the standard FEM package.

**Example 4 (An interface with a corner).** In this example, we explore a heart-shaped interface with a corner as shown in Fig. 11. The analytical level-set function of this heart-shaped interface is given by

$$\gamma(x, y, z) = (x^2 + 9y^2/4 + z^2 - 1)^3 - x^2z^3 - 9y^2z^3/80.$$

The exact solution is given by

$$u(x, y, z) = \begin{cases} \sin(x^2 + y^2 + z^2) & \text{in } \Omega^- := \{(x, y, z) \in \Omega : \gamma(x, y, z) < 0\}, \\ \cos(x^2 + y^2 + z^2) & \text{in } \Omega^+ := \{(x, y, z) \in \Omega : \gamma(x, y, z) > 0\}. \end{cases} \tag{6.5}$$

Note that this function only satisfies the nonhomogeneous jump condition for which the analysis of IFE methods will be given in a forthcoming article. We emphasize that the interface has a corner where the surface is not smooth. So in order to construct IFE functions, the meshes are generated in a manner that the corner only locates at faces not in the interior element. We also note that the constructed exact solutions are smooth in this example. The errors on the heart-shaped surface are shown in the middle plot of Fig. 11 indicating that they are not large around the corner. The convergence behavior of numerical solutions is shown on the right plot of Fig. 11 from which we can observe the optimal convergence clearly for  $L^2$  and  $H^1$  norms.

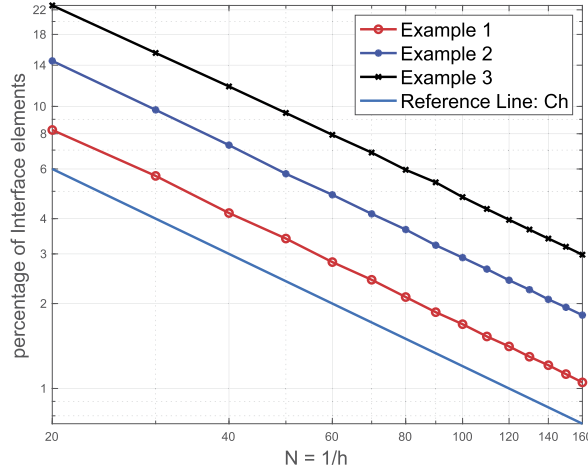


Fig. 10. Percentage of interface elements for Examples 1-3.

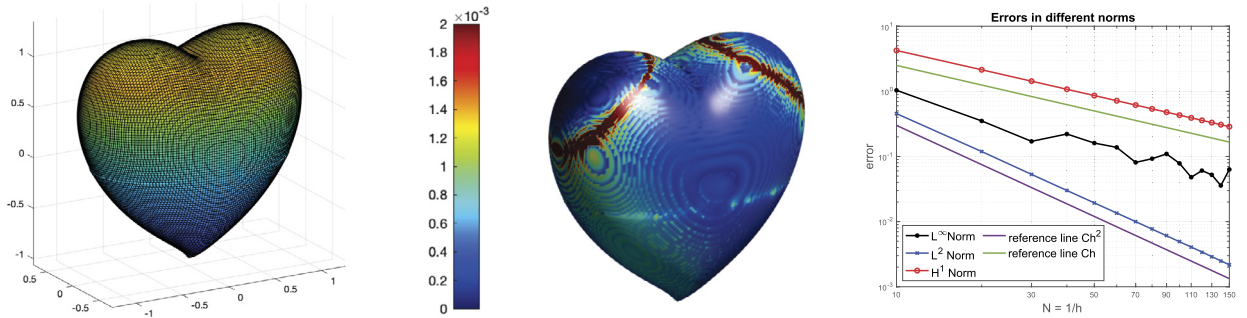


Fig. 11. A plot of the heart-shaped interface (left). The error surfaces of PPIFE solutions (middle). The convergence curves of  $L^2$  and  $H^1$  errors of PPIFE solutions (right).

**Table 2**  
Numerical solution errors and the convergence rates.

	$e_h^0$	Order	$e_h^1$	Order
16	5.6418E-3	NA	5.4544E-1	NA
32	2.0913E-3	1.43	2.5933E-1	1.07
64	5.1039E-4	2.03	1.2048E-1	1.11
128	9.5244E-5	2.42	5.5962E-2	1.11

**Example 5 (A real-world interface: dabbling duck).** In this example, we apply our algorithm to a real-world geometric object, the surface of a dabbling duck shown in Fig. 12. The original data of this interface consists of many cloud points on the surface, as shown in the left plot of Fig. 12. We refer readers to [47] for the availability of the data. We perform the computation on the modeling domain  $\Omega = (0.2, 1) \times (0.2, 1) \times (0.1, 0.9)$  which is large enough to contain all the data points. The fundamental step in the computation is to generate a smooth surface based on the raw data points. Since only the lowest order accuracy is considered in this article, here we generate a signed-distance function by directly computing the distance from nodes in a given mesh to those data points. Then the zero level-set of the signed-distance function is used as the computational interface in this example.

We consider the equation (2.1) with the data  $f = 0$  in  $\Omega$ ,  $u = \sin(3\pi x)\sin(3\pi y)\sin(3\pi z)$  on  $\partial\Omega$  and  $\beta^- = 1, \beta^+ = 10$ . The Cartesian mesh with  $N^3$  cuboids is generated on  $\Omega$  with the mesh size  $N = 16, 32, 64, 128, 256$ . We note that it is difficult to construct a function satisfying the homogeneous jump condition exactly on this complicated real-world interface, so here we shall use the numerical solution computed on the finest mesh  $N = 256$  as the reference solution to compute the errors. The numerical errors and their convergence order are presented in Table 2 where we can observe that the numerical solution errors almost have the expected optimal convergence order in  $L^2$  and  $H^1$  norms. It agrees with the theoretical analysis even for this interface generated from the real-world data.

In addition, we plot the error of IFE solution on  $N = 128$  at the slices at  $y = 0.35, 0.4, 0.45, 0.5, 0.55,$  and  $0.6$  in Fig. 13. We note that the majority of the errors are concentrated on the interface, and the errors are significantly smaller away from the interface. This phenomenon is also observed in the previous examples for which the analytical solutions are available.

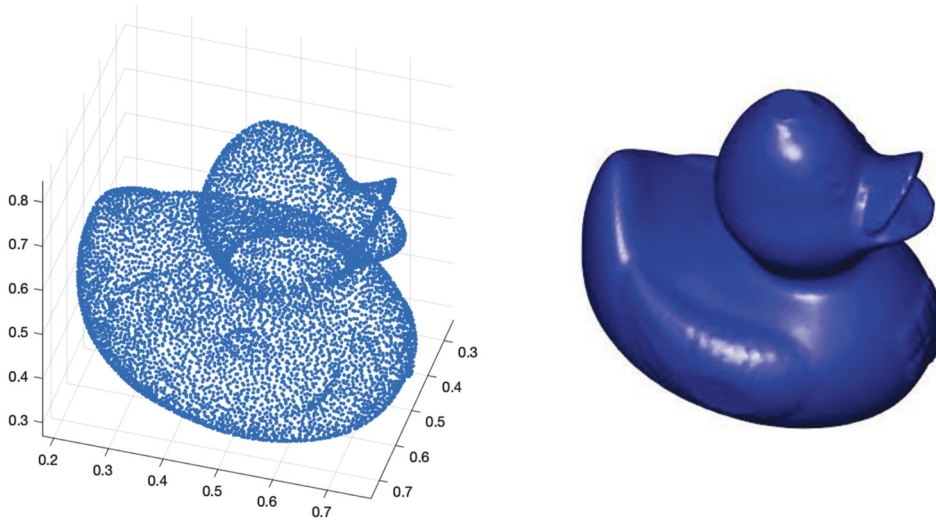


Fig. 12. A duck-shape interface: cloud points (left) and reconstructed smooth interface (right).

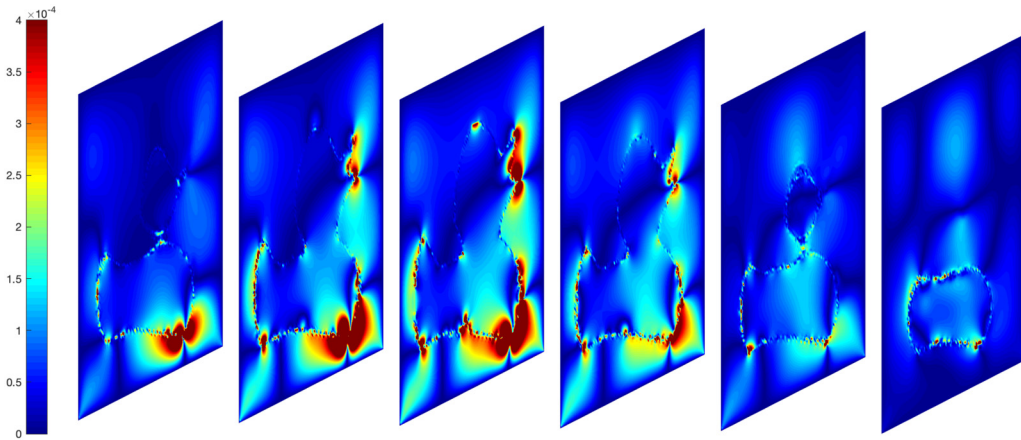


Fig. 13. The slices of errors between  $N = 128$  and  $N = 256$  on  $y = 0.35, 0.4, 0.45, 0.5, 0.55, 0.6$ .

We believe this is due to the advantage of the highly structured mesh, such as the Cartesian mesh, that the IFE method can use to solve interface problems. Furthermore, we note that the duck-shaped interface may have large curvature, especially around the beak and tail. Our computation shows that the maximum curvatures among all cloud points can achieve over 2500. Consequently, the hypothesis (H2) may require a very small mesh size. Certainly, even the finest mesh size  $128^3$  can not achieve the requirement of the hypothesis (H2), but the overall performance of the PPIFE method is still satisfactory. However, we also note that these portions of interface with large curvatures have apparently relatively larger errors. To further investigate how the shape of the interface can affect the errors, we plot the relative errors on the interface in Fig. 14. As indicated by these figures, the errors are concentrated on the portion of the interface including the peak, neck (the lower-right plot in Fig. 14), tail (the lower-left plot in Fig. 14) and the surrounding of the base (the upper-right plot in Fig. 14)). The large curvatures can not be avoided in real-world geometric bodies. How to further enhance the performance of IFE methods on the large-bending surface may require local mesh refinement, i.e., some adaptive mesh strategy for the IFE method [28]. This could be an interesting topic in our future research.

### 7. Conclusions

In this article, we have developed a partially penalized IFE (PPIFE) method for solving elliptic interface problems in three-dimensional space on unfitted meshes. The IFE space is isomorphic to the standard continuous piecewise trilinear finite element space defined on the same mesh, which is independent of the interface location. The penalties are only added on interface faces to handle the discontinuities of IFE functions. We show the PPIFE solutions have optimal convergence rates in both the  $L^2$  and  $H^1$  norm regardless of interface location. Numerical experiments are performed to validate the theoretical estimates for both artificial interface and real-world interface models.

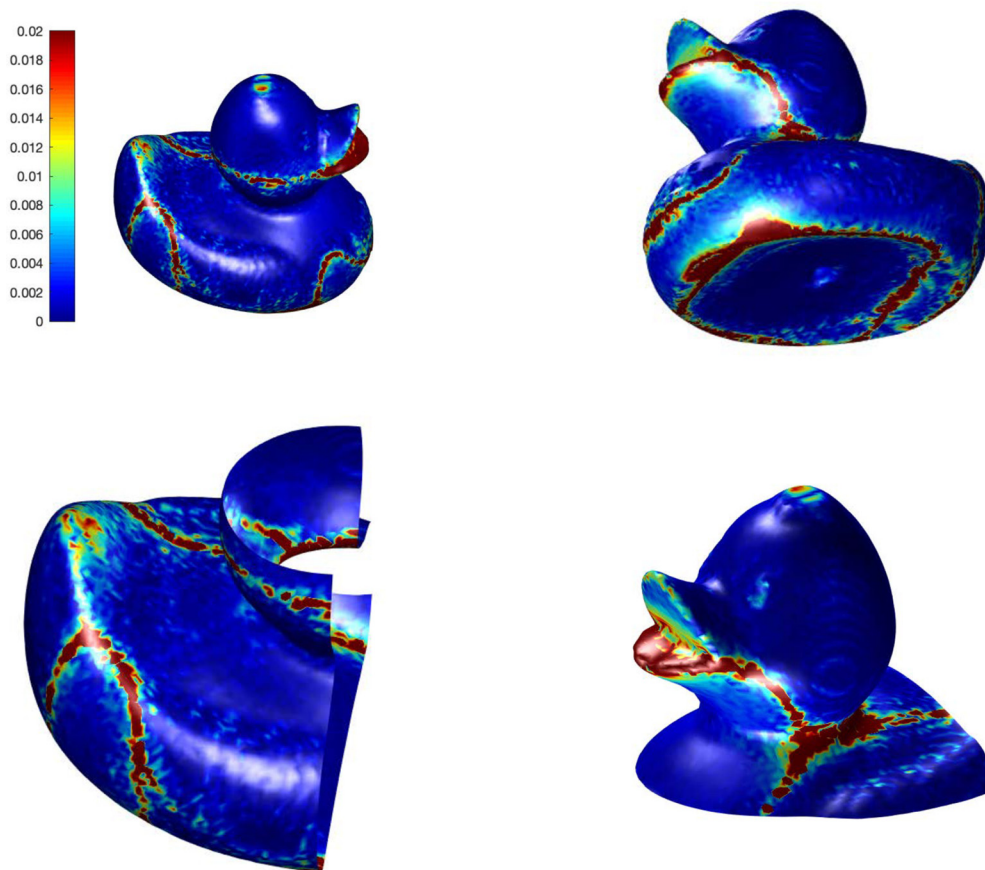


Fig. 14. Relative solution errors of  $N = 128$  on interface.

### CRediT authorship contribution statement

**Ruchi Guo:** Conceptualization, Error Analysis, Writing- Original draft preparation. **Xu Zhang:** Methodology, Computation, Writing- Reviewing and Editing.

### Declaration of competing interest

The authors declare that they have no known competing financial interests or personal relationships that could have appeared to influence the work reported in this paper.

### Acknowledgments

Ruchi Guo is partially supported by National Science Foundation Grant DMS-2012465. Xu Zhang is partially supported by National Science Foundation Grants DMS-1720425, DMS-2005272.

### References

- [1] S. Adjerid, I. Babuška, R. Guo, T. Lin, An enriched immersed finite element method for interface problems with nonhomogeneous jump conditions, 2020.
- [2] S. Adjerid, T. Lin, A  $p$ -th degree immersed finite element for boundary value problems with discontinuous coefficients, *Appl. Numer. Math.* 59 (6) (2009) 1303–1321.
- [3] L. Antiga, J. Peiró, D.A. Steinman, *From Image Data to Computational Domains*, Springer, Milan, Milano, 2009, pp. 123–175.
- [4] D.N. Arnold, F. Brezzi, B. Cockburn, L.D. Marini, Unified analysis of discontinuous Galerkin methods for elliptic problems, *SIAM J. Numer. Anal.* 39 (5) (2002) 1749–1779.
- [5] I. Babuška, A.K. Aziz, On the angle condition in the finite element method, *SIAM J. Numer. Anal.* 13 (2) (1974) 214–226.
- [6] I. Babuška, G. Caloz, J.E. Osborn, Special finite element methods for a class of second order elliptic problems with rough coefficients, *SIAM J. Numer. Anal.* 31 (4) (1994) 945–981.
- [7] E. Bänsch, F. Haußer, O. Lakkis, B. Li, A. Voigt, Finite element method for epitaxial growth with attachment–detachment kinetics, *J. Comput. Phys.* 194 (2) (2004) 409–434.

- [8] E. Burman, S. Claus, P. Hansbo, M.G. Larson, A. Massing, Cutfem: discretizing geometry and partial differential equations, *Int. J. Numer. Methods Eng.* 104 (7) (2015) 472–501.
- [9] W. Cao, X. Zhang, Z. Zhang, Superconvergence of immersed finite element methods for interface problems, *Adv. Comput. Math.* (2017) 1–27.
- [10] L. Chen, H. Wei, M. Wen, An interface-fitted mesh generator and virtual element methods for elliptic interface problems, *J. Comput. Phys.* 334 (1) (2017) 327–348.
- [11] Z. Chen, J. Zou, Finite element methods and their convergence for elliptic and parabolic interface problems, *Numer. Math.* 79 (2) (1998) 175–202.
- [12] C.-C. Chu, I.G. Graham, T.-Y. Hou, A new multiscale finite element method for high-contrast elliptic interface problems, *Math. Comput.* 79 (272) (2010) 1915–1955.
- [13] F. Dassi, S. Perotto, L. Formaggia, P. Ruffo, Efficient geometric reconstruction of complex geological structures, *Math. Comput. Simul.* 106 (2014) 163–184.
- [14] J. Dolbow, N. Moës, T. Belytschko, An extended finite element method for modeling crack growth with frictional contact, *Comput. Methods Appl. Mech. Eng.* 190 (51–52) (2001) 6825–6846.
- [15] H. Federer, Curvature measures, *Trans. Am. Math. Soc.* 93 (1959) 418–491.
- [16] D. Gilbarg, N.S. Trudinger, *Elliptic Partial Differential Equations of Second Order*, vol. 224, 2 edition, Springer, New York, 2001.
- [17] R. Guo, Solving parabolic moving interface problems with dynamical immersed spaces on unfitted meshes: fully discrete analysis, *SIAM J. Numer. Anal.* 2 (59) (2021) 797–828.
- [18] R. Guo, T. Lin, A group of immersed finite element spaces for elliptic interface problems, *IMA J. Numer. Anal.* 39 (1) (2017) 482–511.
- [19] R. Guo, T. Lin, A higher degree immersed finite element method based on a Cauchy extension, *SIAM J. Numer. Anal.* 57 (4) (2019) 1545–1573.
- [20] R. Guo, T. Lin, An immersed finite element method for elliptic interface problems in three dimensions, *J. Comput. Phys.* 414 (1) (2020).
- [21] R. Guo, T. Lin, Y. Lin, A fixed mesh method with immersed finite elements for solving interface inverse problems, *J. Sci. Comput.* 79 (1) (2018) 148–175.
- [22] R. Guo, T. Lin, Y. Lin, Error estimates for a partially penalized immersed finite element method for elasticity interface problems, *ESAIM Math. Model. Numer. Anal.* 54 (1) (2020) 1–24.
- [23] R. Guo, T. Lin, Z. Qiao, Improved error estimation for the partially penalized immersed finite element methods for elliptic interface problems, *Int. J. Numer. Anal. Model.* 16 (4) (2019) 575–589.
- [24] J. Guzmán, M.A. Sánchez, M. Sarkis, Higher-order finite element methods for elliptic problems with interfaces, *ESAIM Math. Model. Numer. Anal.* 50 (5) (2016) 1561–1583.
- [25] J. Guzmán, M.A. Sánchez, M. Sarkis, A finite element method for high-contrast interface problems with error estimates independent of contrast, *J. Sci. Comput.* 73 (1) (2017) 330–365.
- [26] D. Han, P. Wang, X. He, T. Lin, J. Wang, A 3D immersed finite element method with non-homogeneous interface flux jump for applications in particle-in-cell simulations of plasma–lunar surface interactions, *J. Comput. Phys.* 321 (2016) 965–980.
- [27] A. Hansbo, P. Hansbo, An unfitted finite element method, based on Nitsche's method, for elliptic interface problems, *Comput. Methods Appl. Mech. Eng.* 191 (47–48) (2002) 5537–5552.
- [28] C. He, X. Zhang, Residual-based a posteriori error estimation for immersed finite element methods, *J. Sci. Comput.* 81 (3) (2019) 2051–2079.
- [29] X. He, T. Lin, Y. Lin, Approximation capability of a bilinear immersed finite element space, *Numer. Methods Partial Differ. Equ.* 24 (5) (2008) 1265–1300.
- [30] X. He, T. Lin, Y. Lin, X. Zhang, Immersed finite element methods for parabolic equations with moving interface, *Numer. Methods Partial Differ. Equ.* 29 (2) (2013) 619–646.
- [31] R. Hiptmair, J. Li, J. Zou, Convergence analysis of finite element methods for  $H(\text{curl}; \omega)$ -elliptic interface problems, *Numer. Math.* 122 (3) (Nov 2012) 557–578.
- [32] T.Y. Hou, Z. Li, S. Osher, H. Zhao, A hybrid method for moving interface problems with application to the Hele-Shaw flow, *J. Comput. Phys.* 134 (2) (1997) 236–252.
- [33] T.Y. Hou, X.-H. Wu, Z. Cai, Convergence of a multiscale finite element method for elliptic problems with rapidly oscillating coefficients, *Math. Comput.* 68 (227) (1999) 913–943.
- [34] J. Huang, J. Zou, Some new a priori estimates for second-order elliptic and parabolic interface problems, *J. Differ. Equ.* 184 (2) (2002) 570–586.
- [35] R. Kafafy, T. Lin, Y. Lin, J. Wang, Three-dimensional immersed finite element methods for electric field simulation in composite materials, *Int. J. Numer. Methods Eng.* 64 (7) (2005) 940–972.
- [36] R.J. LeVeque, Z. Li, The immersed interface method for elliptic equations with discontinuous coefficients and singular sources, *SIAM J. Numer. Anal.* 31 (4) (1994) 1019–1044.
- [37] Z. Li, The immersed interface method using a finite element formulation, *Appl. Numer. Math.* 27 (3) (1998) 253–267.
- [38] Z. Li, K. Ito, The immersed interface method, in: *Numerical Solutions of PDEs Involving Interfaces and Irregular Domains*, in: *Frontiers in Applied Mathematics*, vol. 33, Society for Industrial and Applied Mathematics (SIAM), Philadelphia, PA, 2006.
- [39] T. Lin, Y. Lin, X. Zhang, A method of lines based on immersed finite elements for parabolic moving interface problems, *Adv. Appl. Math. Mech.* 5 (4) (2013) 548–568.
- [40] T. Lin, Y. Lin, X. Zhang, Partially penalized immersed finite element methods for elliptic interface problems, *SIAM J. Numer. Anal.* 53 (2) (2015) 1121–1144.
- [41] T. Lin, D. Sheen, X. Zhang, A nonconforming immersed finite element method for elliptic interface problems, *J. Sci. Comput.* 79 (1) (2019) 442–463.
- [42] T. Lin, X. Zhang, Linear and bilinear immersed finite elements for planar elasticity interface problems, *J. Comput. Appl. Math.* 236 (18) (2012) 4681–4699.
- [43] J.M. Melenk, I. Babuška, The partition of unity finite element method: basic theory and applications, *Comput. Methods Appl. Mech. Eng.* 139 (1–4) (1996) 289–314.
- [44] J. Morvan, B. Thibert, On the approximation of a smooth surface with a triangulated mesh, *Comput. Geom.* 23 (3) (2002) 337–352.
- [45] C.S. Peskin, The immersed boundary method, *Acta Numer.* 11 (2002) 479–517.
- [46] B. Rivière, *Discontinuous Galerkin Methods for Solving Elliptic and Parabolic Equations. Theory and Implementation*, *Frontiers in Applied Mathematics*, vol. 35, Society for Industrial and Applied Mathematics (SIAM), Philadelphia, PA, 2008.
- [47] M. Rouhani, A.D. Sappa, Implicit b-spline fitting using the 3l algorithm, in: *18th IEEE International Conference on Image Processing*, 2011, pp. 893–896.
- [48] S. Vallaghé, T. Papadopoulos, A trilinear immersed finite element method for solving the electroencephalography forward problem, *SIAM J. Sci. Comput.* 32 (4) (2010) 2379–2394.
- [49] F. Wang, Y. Xiao, J. Xu, High-order extended finite element methods for solving interface problems, arXiv:1604.06171v1, 2016.
- [50] T. Warburton, J.S. Hesthaven, On the constants in  $hp$ -finite element trace inverse inequalities, *Comput. Methods Appl. Mech. Eng.* 192 (25) (2003) 2765–2773.
- [51] Q. Zhang, Z. Li, Z. Zhang, A sparse grid stochastic collocation method for elliptic interface problems with random input, *J. Sci. Comput.* 67 (1) (2016) 262–280.
- [52] Y.C. Zhou, S. Zhao, M. Feig, G.W. Wei, High order matched interface and boundary method for elliptic equations with discontinuous coefficients and singular sources, *J. Comput. Phys.* 213 (1) (2006) 1–30.